

RADC-TR-82-130 Final Technical Report May 1982



HOLOGRAPHIC ALIGNMENT BREADBOARD

Hughes Aircraft Company

Sponsored by Defense Advanced Research Projects Agency (DoD) ARPA Order No. 3503

APPROVED FOR PUBLIC RELEASE: DISTRIBUTION UNLIMITED



The views and conclusions contained in this document are those of the authors and should not be interpreted as necessarily representing the official policies, either expressed or implied, of the Defense Advanced Research Projects Agency or the U.S. Government.

> ROME AIR DEVELOPMENT CENTER **Air Force Systems Command** Griffiss Air Force Base, NY 13447

This report has been reviewed by the RADC Public Affairs Office (PA) and is releasable to the National Technical Information Service (NTIS). At NTIS it will be releasable to the general public, including foreign nations.

RADC-TR-82-130 has been reviewed and is approved for publication.

PPROVED:

JAMES W. CUSACK Project Engineer

James Cusach

APPROVED: Sein Ellh

LOUIS E. WHITE, Lt Col, USAF Acting Chief, Surveillance Division

FOR THE COMMANDER: John P. Kluss

JOHN P. HUSS Acting Chief, Plans Office

If your address has changed or if you wish to be removed from the RADC mailing list, or if the addressee is no longer employed by your organization, please notify RADC. (OCSE) Griffiss AFB NY 13441. This will assist us in maintaining a current mailing list.

Do not return copies of this report unless contractual obligations or notices on a specific document requires that it be returned.

HOLOGRAPHIC ALIGNMENT BREADBOARD

D. L. Sullivan

Contractor: Hughes Aircraft Company Contract Number: F30602-79-C-0228

Effective Date of Contract: 1 August 1979 Contract Expiration Date: 1 June 1981

Short Title of Work: Holographic Alignment Breadboard Program Code Number: 0E20

Period of Work Covered: Aug 79 - Jun 81

Principal Investigator: D. L. Sullivan

Phone: 213 616-4705

James W. Cusack Project Engineer:

Phone: 315 330-3145

Approved for public release; distribution unlimited.

This research was supported by the Defense Advanced Research Projects Agency of the Department of Defense and was monitored by James W. Cusack (RADC/OCSE), Griffiss AFB NY 13441 under Contract F30602-79-C-0228.

UNCLASSIFIED

SECURITY CLASSIFICATION OF THIS PAGE (When Date Entered)

REPORT DOCUMENTATI		READ INSTRUCTIONS BEFORE COMPLETING FORM
T. REPORY NUMBER	1 -	1. RECIPIENT'S CATALOG NUMBER
RADC-TR-82-130	ADA120	
L. TITLE (and Subtitle)		Final Technical Report
HOLOGRAPHIC ALIGNMENT BREADBO	ADD	7 Aug 79 - 30 Jun 81
HOLOGRAPHIC ALIGNMENT BREADS		6. PERFORMING O'TG. REPORT NUMBER
	$H \Lambda 0$	FR81-72-1029
7. AUTHOR(s)		S. CONTRACT OR GRANT NUMBER(s)
D. L. Sullivan		F30602-79-C-0228
		130002=79=0=0228
PERFORMING ORGANIZATION NAME AND ADDR	RESS	10. PROGRAM ELEMENT, PROJECT, TASK AREA & WORK UNIT NUMBERS
Hughes Aircraft Company		62301E
Centinela and Teale Streets		C5030102
Culver City CA 90230 1. CONTROLLING OFFICE NAME AND ADDRESS		12. REPORT DATE
Defense Advanced Research Pro	iects Agency	May 1982
1400 Wilson Blvd		13. NUMBER OF PAGES
Arlington VA 22209 4. MONITORING AGENCY NAME & ADORESS(11 die		140
		15. SECURITY CLASS. (of this report)
Rome Air Development Center (OCSE)	UNCLASSIFIED
Griffiss AFB NY 13441	•	164. DECLASSIFICATION/DOWNGRADING
		N/ACHEOULE
7. DISTRIBUTION STATEMENT (of the abstract ent	erad in Black 20, if different fre	m Report)
Same .		
SUPPLEMENTARY NOTES		
RADC Project Engineer: James	W. Cusack (OCSE)	
. KEY WORDS (Continue en reverse side if necessar	y and identify by block number)	
Holographic Gratings		
Laser Pointing Systems		
. ABSTRACT (Continue on reverse side if necessary	and identify by block number)	
Previous studies have shown th		unlinear orating on the
primary mirror of a laser bear	pointing system.	The nonlinear orating of
focus a full aperture sample (of the laser beam	or an alignment beam to a
conveniently located alignment	sensor, where it	is used for wavefront
error diagnostic and control	Durnoses The Ho	lagraphia Aliannana Burat

error diagnostic and control purposes. The Holographic Alignment Breadboard (HOLAB) program designed, fabricated, and tested the holographic grating laser beam sampler alignment technique just described. A bread-

DD 1 JAN 73 1473 EDITION OF 1 NOV 65 IS DESOLETE

UNCLASSIFIED

SECURITY CLASSIFICATION OF THIS PASE(When Date Entered

board system was built which incorporated an ox-axis primary mirror with a 30 centimeter diameter and an F-number of F/1.5. Tests were conducted with the breadboard to establish the operational properties of this technique. The experimental data correlated well with analytical predictions.

		_
Access	ion For	
NTIS DTIC T		
Unanno	ounced	
Justii	ication_	
-		
Distr	ibution/	
	lability	Codes
	Avail an	
Dist	Specia	1
1		
Ш	1 1	
י ען	1	

COPY

UNCLASSIFIED

SECURITY CLASSIFICATION OF THIP PAGE(When Date Entered)

PREFACE

This is the final report prepared by the Hughes Aircraft Company under Contract F30602-79-C-0228 covering 7 August 1979 through 30 June 1981. The work was performed for the Rome Air Development Center, Griffiss AFB, New York, with Lt. George Fernandez and Mr. Jim Cusack acting as project officers.

This report was compiled by Mr. D. L. Sullivan from technical contributions by the following persons:

Mr. L. P. Allum

Mr. A. Au

Mr. M. Carey

Mr. C. C. DeAnda

Mr. H. Garvin

Dr. M. I. Greenfield

Dr. T. L. Holcomb

Mr. B. F. Hower

Ms. I. Jimenez

Mr. R. K. Kimmel

Mr. J. A. Levy

Mr. D. K. Neihart

Mr. W. A. Rosser, Jr.

Dr. E. J. Rudisill

Mr. P. D. Shubert

Mr. D. L. Sullivan

Mr. D. E. Vandenberg

Dr. R. J. Withrington

Dr. N. Wu

CONTENTS

I	INT	RODUCTION AND SUMMARY
	1.1 1.2 1.3 1.4 1.5	Background
11	BRE	ADBOARD DESIGN
	2. 1	Optical Design 8
		2. 1. 1 Introduction and Summary
	2. 2	Mechanical Design
		2. 2. 1 Introduction
	2.3	Servo and Controls Design
		2.3.1 Introduction
m	HOL	OGRAPHIC GRATING FABRICATION
	3. 1 3. 2	Introduction
		3. 2. 1 Concept
		30 cm Diameter f/1.5 Parabolic Mirror 68
	3.3	Holographic Exposure
		3.3.1 Holographic Grating Construction Optics Design 72 3.3.2 Exposure Configuration
	3. 4 3. 5	Ion Beam Etching

CONTENTS (Continued)

	3.6	Holographic Grating Performance 83
		3. 6. 1 Diffraction Analysis
IV	EXP	ERIMENTAL RESULTS 94
	4. 1	Experimental Procedures
	4. 2	Wavefront Quality Measurements
		4. 2. 1 Nominal System
		4. 2. 2 Focus Effects
		4.2.3 Decenter Effects
		4. 2. 4 Off-Axis Steering Effects
		4. 2. 5 Substrate Deformation Effects

LIST OF ILLUSTRATIONS

Figure		Page
1	Holographic Grating Full-aperture Beam Sampling	_
	for Wavefront and LOS Control	2
2	HOLAB Optical Schematic	4
3	HOLAB Breadboard	5
4	HOLAB Optical System	9
5	Focal Length Adjustment of Vertex Lens and LOS	
	Control	12
6	Reference Beam Centroid Shift Sensitivity Study	13
7	Input Laser Beam and Return Sample Beam Footprints on the Folding Mirror	14
8	Outer Ray Clearance Tradeoff at Fold Mirror	15
9	Inner Ray Clearance Tradeoff at Fold Mirror	17
10	Wave Front Aberration for the Outgoing Laser Beam and the Sample Beam ($\lambda = 0.6328 \mu m$)	19
11	Wave Front Contour Comparison between Outgoing Laser Beam and Sample Beam	20
12	Beam Expander	28
13	Mirror, Reference Flat	29
14	Folding Flat Mirror	29
15	HOLAB Breadboard	34
16	Primary Mirror Mount	36
17	Primary mirror deformation device	36
18	lg LOS Gravity Load	37
19	Single-point Edge Loading	3.
20	Single-point Intermediate Loading, Case A	38
21	Single-point Intermediate Loading, Case B	38
22	Single-point Intermediate Loading, Case C	39
23	Single-point Intermediate Loading, Case D	39
24	Single-point Intermediate Loading, Case E	40
25	Single-point Intermediate Loading, Case F	41
26	Three-point Loading	41
27	Six-point Loading	41
29	Twelve-point Loading	42

LIST OF ILLUSTRATIONS (Continued)

Figure		Page
29	Three-point Edge Loading	42
30	Reference Beam Laser Mounted on Reference Flat (side view)	44
31	Reference Beam Laser Mounted on Reference Flat (top view)	45
32	Collimating Lens Assembly	46
33	Collimating Lens/Steering Mirror 3 Assembly	47
34	Steering Mirror/Galve Assembly	49
35	Detector Mount	50
36	Angle Sensor Electronics	56
37	HOLAB Electronics Functional Block Diagram	57
38	Basic Surface Grating Fabrication Steps	61
39	Dip Draining Parameters	62
40	Dip Draining Photoresist Deposition System Schematic	64
41	HOLAB Dip Draining Photoresist Coating System Hardware	64
42	Photoresist Exit Flow Rate Veriation in Deposition Tank	65
43	Exit Flow Rate Effects on Venturi Differential Pressure Indications	67
44	Control Subsystem Capability to Maintain Constant Differential Pressure	67
45	Contact Angle Variation for the HOLAB Mirror	69
46	Variation in Substrate Coating Rate for Fixed Vertical Rate	69
47	Variation in Substrate Cross Sectional Area	70
48	Photoresist Thickness Profile on HOLAB Primary Mirror with Constant Differential Pressure (ΔP) Control	72
49	Holographic Grating Construction Optics Configuration	73
50	HOLAB Holographic Grating Exposure System	77
51	Ion Beam Etching System Used for HOLAB	80
52	Diffraction Grating Groove Model	84
53	Holographic Grating Frequency Vergus Rading	84
54	HOLAR Measurement Schematic	RR

LIST OF ILLUSTRATIONS (Continued)

Figure		Page
55	Subaperture Measurement Locations on the	
	HOLAB Grating	89
56	Grating Efficiency Measurements	92
57	HOLAB Grating Efficiency	93
58	HOLAB Optical Schematic	95
59	Modifications for Output Beam Interferograms	97
60	Nominal System Output Beam Interferograms (Double Pass).	98
61	Nominal System Sample Beam Interferograms (Single Pass).	98
62	Primary Mirror Interferograms	99
63	Beam Expander Interferograms	100
64	Secondary Mirror and Collimating Lens Focus Effects	102
65	Focus Effects in Sample Beam Due to Collimating Lens Longitudinal Motion (Secondary Mirror Fixed at Infinity	
	Focus)	103
66	Focus Effects, Secondary Mirror Only	104
67	Focus Effects, Secondary Mirror and Collimating Lens Move Together	105
68	Seconds Mirror and Collimating Lens Lateral Translation Effects	106
69	Secondary Mirror and Collimating Lens Lateral Translation Effects	107
70	Collimating Lens Lateral Translation Effects on Sample Beam	109
71	Decenter Effects, Secondary Mirror Only	110
72	Decenter Effects, Secondary Mirror and Collimating	
,-	Lens Move Together	111
73	Decenter Effects, Collimating Lens Only	112
74	Beam Expander Off-axis Steering Effects	113
75	Off-axis Steering Effects	114
76	Primary Mirror Substrate Deformation Effects	115
77	Primary Mirror Deformation Device Locations	116
78	Primary Mirror Substrate Deformation	117

LIST OF TABLES

	Page
HOLAB Optical Characteristics	10
LOS Accuracy Evaluation	22
Confocal Parabola Separation and LOS Accuracy	22
Sample Beam Collimating Optics Manufacturing Sensitivities	23
Sample Beam Collimating Optics Alignment Sensitivities	24
Collimating Optical Adjustment Sensitivities	25
Collimating Lens Optical Adjustment Ranges Required	26
Vertex Lens Tolerance	26
Reflectance and Transmittance of HOLAB Optical Components	31
Beamsplitting Ratios for HOLAB Components	32
Detector and Interferogram Plane Energy Levels	54
Variation in Substrate Coating Rage with Constant Exit Flow	71
Construction Otpics Manufacturing Sensitivities	74
Construction Otpics Alignment Sensitivities	75
Theoretical Diffraction Efficiencies as a Function of Aperture Location	85
Diffraction Efficiency of the Outgoing Beam (Zero Order) as a Function of Radial Position	86
Diffraction Angle and Efficiency as a Function of Diffraction Order	87
Efficiency Data	90
System Wavefront Errors; Departures from Ideal Wavefronts	100

SECTION I INTRODUCTION AND SUMMARY

1.1 BACKGROUND

An earlier ARPA funded holographic grating study* demonstrated that a nonlinear (i.e., curved and unequally spaced) grating could be placed on the primary mirror of a laser beam pointing system to focus a sample of the beam to a conveniently located alignment sensor. With this approach, the full beam wavefront can be sampled. Also, because the primary mirror is the last element in the optical train of the outgoing beam, the wavefront error of the entire optical train is imprinted on the sampled beam. This beam can then be used for wavefront error diagnostic and control purposes. It should be noted that rather than sampling the high-energy laser (HEL) beam itself, the typical utilization is to sample an alignment beam (typically at 0.6328 micrometers) which traverses the same optical path as the HEL beam.

The method by which the sampled beam from a holographic grating on the primary mirror of a laser pointing system can be used for wavefront and line-of-sight (LOS) control is illustrated conceptually in Figure 1. The sensor package itself cannot serve as a LOS reference, particularly when steering off-axis. Hence, an inertially stabilized reference beam is added to the system, which when focused on the sensor detector plane serves as the inertial pointing reference. The sample beam from the holographic grating is also focused on the sensor detector plane. If the beams focused position does not correspond to the reference beam position, then the outgoing beam is not properly aligned to the desired inertial pointing reference direction. An error signal proportional to the displacement between the sample and reference beam will drive the beam steering mirror until the displacement is zero. The outgoing beam will then be inertially stabilized and aligned to the desired pointing direction.

^{*}Holographic Grating Study Report, Vol. I, Hughes Aircraft Company, Contract No. F30602-76-C-0402, August 1978.

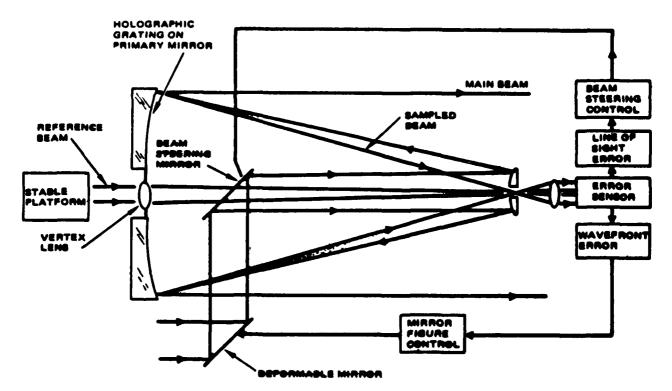


Figure 1. Holographic groting full-aporture beam sampling for wavefront and les control.

1.2 OVERVIEW

The objectives of the Holographic Alignment Breadboard (HOLAB) program were to design, fabricate, and test the holographic grating laser beam sampler alignment technique described above. A breadboard system was designed and fabricated which incorporated an on-axis primary mirror with a 30-centimeter diameter and an F-number of F/1.5. Tests were conducted with the breadboard to establish the operational properties of this sampler alignment technique. Angle sensor test results provide a data lase of experimental measurements for the ability of a holographic grating to correctly sense beam steering performance. In addition, interferometric measurements of the wavefront relationships of the outgoing beam and the sample beam assess the wavefront aberration sensing capabilities of this technique.

The HOLAB program involved the development and testing of a holographic beam sampler alignment Breadboard Model within six principal tasks:

- 1. The first task was to design the breadboard, develop the experimental plan for establishing its performance, and define the performance criteria to quantify the experimental results.
- 2. The second task involved the fabrication of the breadboard.
- 3. The third task was the preliminary check-out of the breadboard.
- 4. The fourth task implemented pointing error measurements of the outgoing beam while the sampled beam and reference beam are servo controlled to be coincident on a common angle detector. These data support the pointing direction measurement capabilities of the holographic sampling technique.
- 5. The fifth task implemented interferometric measurements of main and sampled beams to determine their wavefront relationships in support of wavefront aberration sensing by holographic sampling approaches.
- 6. The sixth task established the operational properties of the breadboard from the experimental results in terms of beam wavefront and alignment sensing and control.

1.3 BREADBOARD SCHEMATIC

The optical schematic of the HOLAB program breadboard is shown in Figure 2. Important features of the breadboard are:

- l. Automatic closed-loop tilt control of the input beam in azimuth and elevation.
- 2. Off-axis steering control of ±2 milliradians by manual rotation of the reference flat as well as the reference beam laser and expander which are mounted to it.
- 3. Manual focus and x-y translation of the secondary mirror and/or collimating lens for alignment effect studies.
- 4. Manual strain mechanisms behind the primary mirror for mirror deformation effect studies.
- 5. Provisions for producing interferograms of the sampled beam and autocollimated outgoing beam for wavefront phase comparison measurements.
- 6. Angle detectors for measuring angular deviations of the outgoing beam, sample beam, and reference beam.

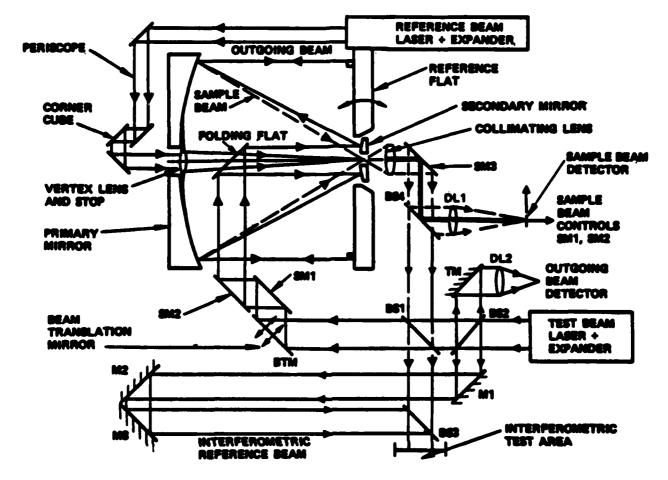


Figure 2. HOLAB optical schematic.

The reference flat autoreflects the outgoing beam back through the beam expander and permits the pointing angle and phase profile of the outgoing beam to be measured with convenient sized optical components. The reference flat is located forward of the secondary mirror so that the support and displacement mechanism for the secondary mirror and collimating lens do not obscure the beam expander aperture.

A photograph of the HOLAB Breadboard hardware is given in Figure 3.

1.4 PRINCIPAL ACCOMPLISHMENTS

The significant results of the HOLAB program include the following:

1. First Holographic Grating in a Beam Control Configuration. The HOLAB holographic grating was fabricated on an f/1.5, 30 centimeter diameter paraboloidally figured primary mirror. The

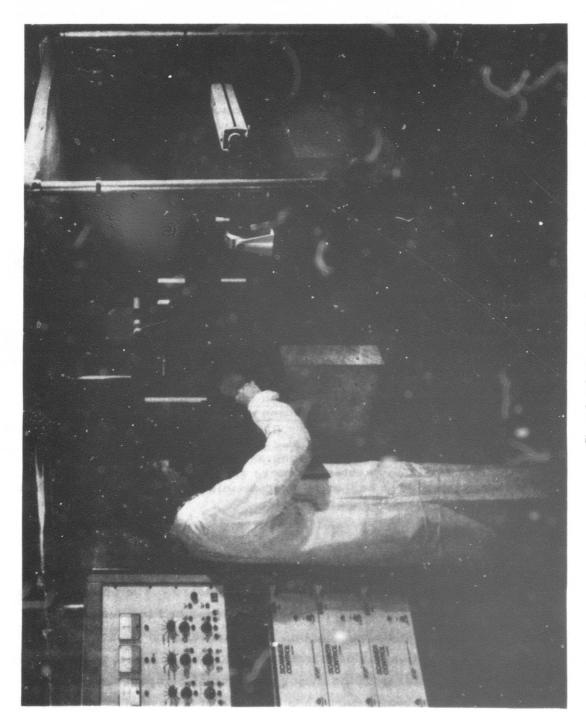


Figure 3. HOLAB breadboard.

beam sampling configuration (sample beam focused near the vertex of the secondary mirror of an afocal beam expander) is the same as that which would most likely be designed for a beam control system of any scale. The HOLAB holographic grating is the first known hardware application which utilizes this beam control configuration.

- 2. Predicted Holographic Grating Sampling Efficiency Achieved.

 The ability to achieve the predicted sampling efficiency confirms the analytical accuracy of the diffraction codes. In addition, the controllability of the various fabrication processes required to produce the holographic grating was demonstrated.
- 3. Experimental Data Correlates Well with Analytical Predictions. The wavefront perturbations and pointing error measurements measured with the HOLAB breadboard correlated well with analytical predictions. This important outcome confirmed the validity of the analytical techniques used for performance predictions.
- 4. Data Confirms Necessity for Alignment Control of the Collimating

 Lens Assembly. The experimental data show that measurement
 accuracy limitations are created by misalignments of the collimating lens assembly. This misalignment adds coma to the
 sample beam which does not exist on the outgoing beam. Hence,
 false output wavefront aberration errors and coma-induced pointing
 errors are implied by the sample beam wavefront sensor measurements. System design techniques for controlling these errors are
 available.
- 5. Ultimate Measurement Precision of this Technique Exceeded the Current Measurement Resolution of the HOLAB Breadboard.

 Optical figuring errors on the primary mirror surface and residual aberration in the nominally aligned system sample beam limited HOLAB data measurement accuracies. These limitations can be reduced in any system by more stringent allocation of fabrication tolerances and/or by precise initial "static-error" calibration of wavefront sensors used.

1.5 REPORT ORGANIZATION

Section II, Breadboard Design, details the analytical design efforts which preceded the fabrication of the HOLAB breadboard. The optical design and tolerancing of the breadboard components is described in Section 2.1. In addition, system radiometric, imaging, and pointing performance predictions are recorded. Section 2.2 describes the mechanical layout of the breadboard and the design features of the major mechanical components. Section 2.3 discusses the servo performance analysis of the breadboard and the design features of the major servo hardware components.

Section III, Holographic Grating Fabrication, discusses the processes required to fabricate the holographic grating on the surface of the HOLAB primary mirror. In addition, performance predictions and measured data are also described.

Section IV, Experimental Results, discusses the reduced experimental data which were obtained with the HOLAB breadboard and compares these measurements to analytical predictions.

SECTION II BREADBOARD DESIGN

2.1 OPTICAL DESIGN

2.1.1 Introduction and Summary

The HOLAB optical system, Figure 4, consists of (1) an 8X confocal parabolic beam expander, (2) a low efficiency holographic grating on the primary mirror to diffract a small portion of the incident beam as a sample beam focused at the vertex of the secondary mirror, (3) a collimating lens group that collimates the sample beam such that sample beam diameter is close to that of the input laser beam, and (4) a collimated reference beam that is focused by the vertex lens at the vertex of the primary mirror to the same spot where the sample beam is focused. The collimated sample beam is used to monitor beam quality. The sample beam, together with the reference beam, is used to control line-of-sight (LOS).

The HOLAB optical design task was to (1) perform system tradeoffs in the areas of FOV, obscuration, and vignetting; (2) perform detailed design of all the optical components including the holographic grating construction optical elements; (3) make performance evaluation in terms of OPD maps and centroid linearity; (4) determine optical tolerance and associated necessary alignment adjustments; and (5) provide optical element drawings, optical system layout and holographic grating construction optical layout.

Performance goals for the design effort were that the sample beam wavefront should match the outgoing laser wavefront to within one wave peak-to-valley at 0.6328 microns for the entire ±2 mrad FOV in output space and that LOS control accuracy should be within 1 µrad between the reference beam and outgoing laser beam centroids over the ±2 mrad FOV. The system design meets these performance goals. Its optical characteristics are given in Table 1.

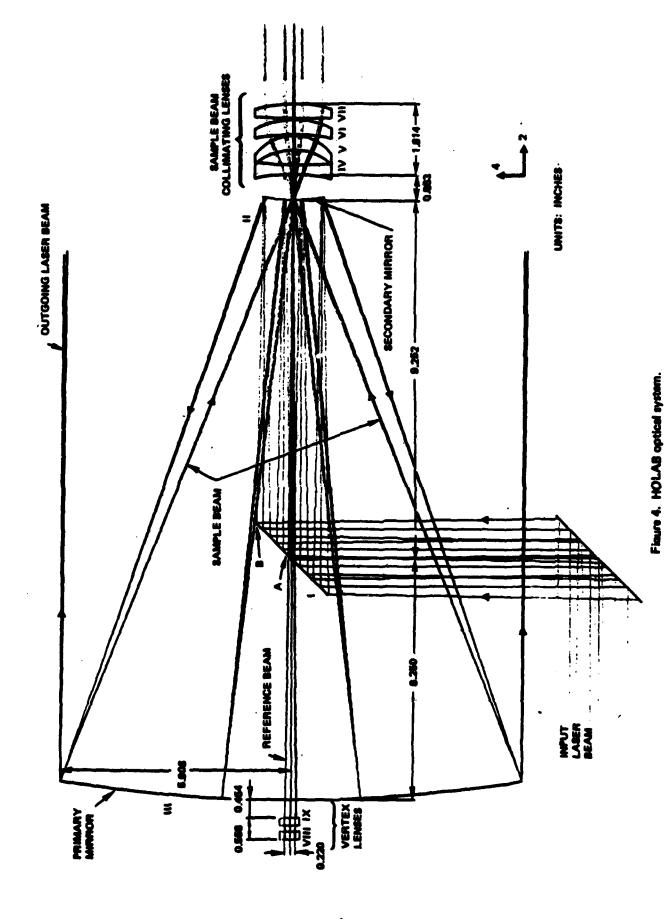


TABLE 1. HOLAB OPTICAL CHARACTERISTICS

Afocal Beam Expander	
Afocal Magnification	8X
Primary Mirror Aperture	11.811 inches
Primary Mirror F-number	F/1.5
Separation Between Primary Mirror and	
Secondary Mirror	15.502 inches
FOV	±2 mrad
Primary Mirror Linear Obscuration	0.3
Sample Beam Optics	
Holographic Grating EFL	15.502 inches
Collimating Optics EFL	1.880 inches
Afocal Magnification	8X
Collimating Optics F-Number	1. 27
Collimating Optics FOV	±16 mrad
Reference Beam Optics	
EFL	15.502 inches
F-number	70.5
FOV	±2 mrad
Wavelength (all beams)	0.6328 micron

2.1.2 Optical Design Details

This discussion of the optical design is divided into three subsections:
(1) sample beam collimating lens design, (2) reference beam vertex lens characteristics and design, and (3) folding mirror position and system obscuration considerations.

Sample Beam Collimating Lens Design. The sample beam diffracted from the holographic grating has a large amount of comatic aberration because the speed of the combination of the primary mirror reflecting power and the holographic grating diffracting power is very fast (F/0.7). The main goal of the collimating lens design is to correct the comatic aberration of the sample beam. The collimating lens group (Figure 4) consists of four spherical lenses with a negative lens closest to the secondary mirror and a three positive element closely spaced lens group. The collimating lens also

collimates the sample beam to have the same diameter as that of the input laser beam, so that an interferogram of the sample beam can be produced.

The collimating lens optical parameters together with the construction optical parameters initially were optimized so that the spherical and comatic aberrations of the collimated sample beam were minimal. Finally all optical parameters were optimized to match the wave aberrations of the sample beam to that of the outgoing laser beam to within one wave peak-to-valley at 0.6328 micron for all field angles.

Reference Beam Vertex Lens Characteristics and Design. The reference beam is used with the sample beam to control LOS so that the outgoing laser beam is parallel to the reference beam within an accuracy of 1 µrad. This condition can be achieved by using a reference beam vertex lens with the identical focal length as the hologram on a first order optics basis (Figure 5). The wavefront aberration of the sample beam caused the centroids of the sample beam to shift slightly from that of the reference beam for different field angles. If the focal length of the vertex lens of the reference beam is adjusted, the centroids of the reference beam can track those of the sample beam if the sample beam centroid shifts are linear with respect to field angle.

The design of the reference beam vertex lens consists of a negative and positive lens pair with adjustable spacing between the lenses. This design provides a focal length adjustment capability, and hence, avoids overly tight fabrication tolerances. It also permits spacing between the vertex lens and primary mirror vertex to be obtained for inclusion of an aperture stop physically at the vertex. The tradeoffs between the centroid shift sensitivity and the power of the negative lens element with the lens separation as parameter are shown in Figure 6. The centroid shift sensitivity is strongly influenced by the power of the negative lens and is relatively insensitive to the spacing between the lenses. The design point was selected at a moderate centroid shift sensitivity of 0.76 μ rad/mil (30 μ rad/mm) at the extremes of the \pm 2 mrad FOV. The lens separation is 0.157 inch (0.4 cm) so that a focal length adjustment on the order of \pm 5 percent can be made.

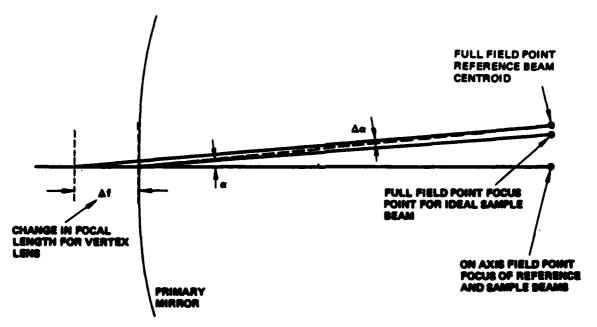


Figure 5. Focal length adjustment of vertex lens and LOS control.

Folding Mirror Position and System Obscuration. The folding mirror between the primary and the secondary mirrors directs the outgoing beam from the laser source into the 8X beam expander as shown in Figure 4. This folding mirror must have sufficient area to reflect the centrally obscured beam onto the secondary mirror without any vignetting. Because of the 4 mrad FOV in output space, the outgoing beam will wander on this folding mirror; the extent of the beam wander is shown in Figure 7. The outer area is visibly larger than the extent of the input laser beam, but the folding mirror reflecting area should not be extended to block the return sample beam from reaching the secondary mirror vertex, Figure 4. Also, the center unused mirror area is much smaller than the centrally obscured portion of the incoming beam. The central unused portion of the folding mirror will be made into a hole for the reference beam to pass through.

If the folding mirror is placed too close to the secondary mirror, the return sample beam will be blocked by the folding mirror. Two sets of curves for the 8X HOLAB system, with FOV and linear obscuration as parameters, are shown in Figure 8. The solid lines correspond to the extreme point of the laser beam (B in Figure 4) on the folding mirror closest to the secondary mirror. The dashed lines correspond to the minimum clearance required for the return sample beam to clear the folding mirror. For the present HOLAB system with 0.3 linear obscuration of the

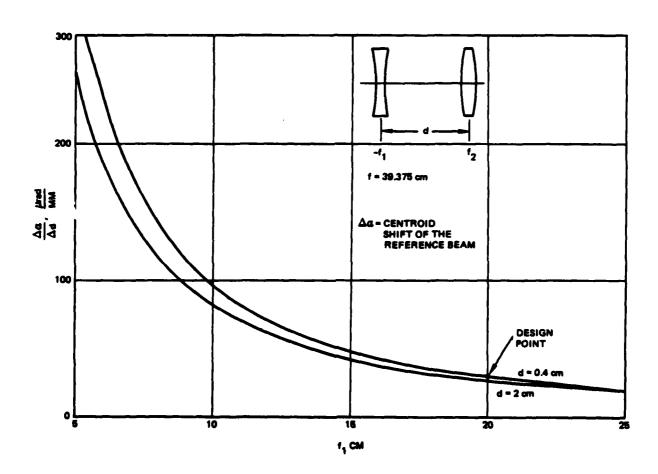


Figure 6. Reference beam controld shift sensitivity study.

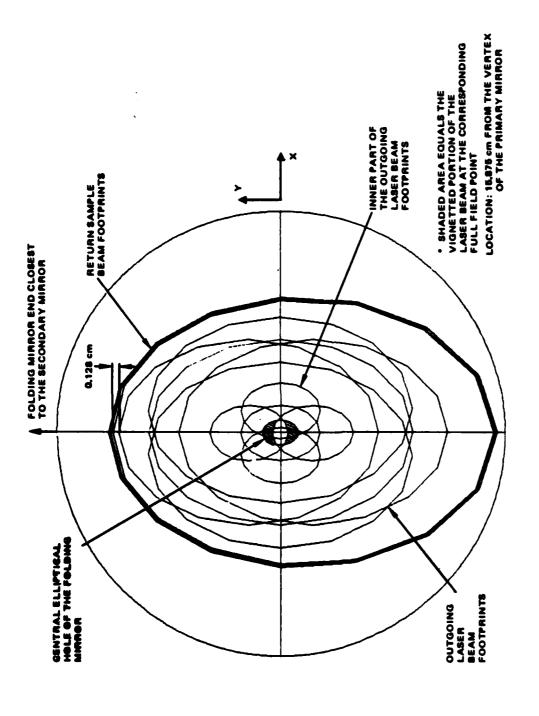


Figure 7. Input laser beam and return sample beam footprints on the folding mirror.

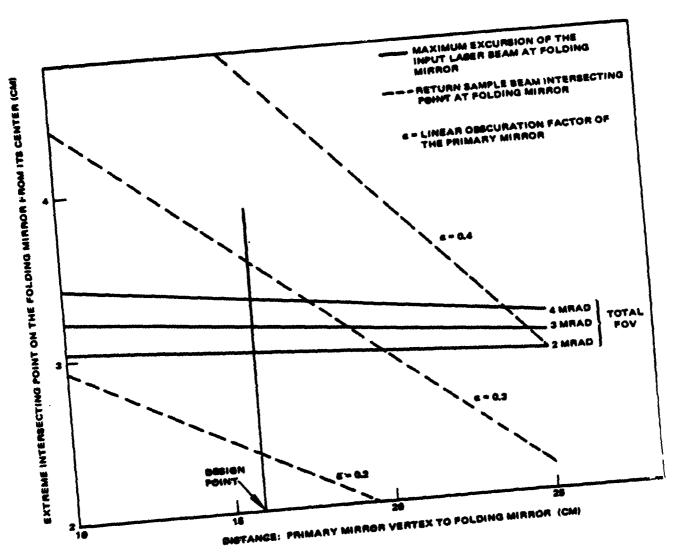


Figure 8. Outer ray clearance trade-off at fold mirror.

laser beam and 4 mrad FOV, the folding mirror cannot be placed more than 6.890 inches (17.5 cm) from the vertex of the primary mirror. The set of curves in Figure 9 relate the maximum unused central linear dimension of the folding mirror to the position of the folding mirror; the curves correspond to different values of the linear laser obscuration ratio and to the beam steering FOV. The unused area must be large enough to take care of mirror hole roll-off and reference beam wander due to its 4 mrad FOV.

For the 0.3 linear obscuration and 4 mrad FOV HOLAB system, the near optimum position of folding mirror is about 6.496 inches (16.5 cm) from the primary mirror vertex. At this position, the closest separation between the return sample beam and the outgoing laser beam at the folding mirror is 0.079 inch (0.2 cm) wide along the X axis. After allowing full FOV reference beam wander with a reference beam size of 0.094 inch (0.24 cm) in diameter at the vertex of the primary mirror, the closest separation between the input laser beam and the reference beam at the folding mirror is 0.006 inch (0.15 cm).

The clearances given above correspond to limit ray intercepts in the plane of the fold mirror and do not allow for fold mirror positional tolerances or chamfers. Since the ray clearances are tight; a compromise between FOV, obscuration ratio and vignetting is recommended. Also the fold mirror is relatively much closer to the secondary mirror than in actual HEL system configurations. Moving the fold mirror back eases the outer ray clearances but further reduces the reference beam size for no vignetting.

Due to the mirror roll-off and mirror position tolerance considerations, the limiting ray of the outgoing laser beam was set at least 0.020 inch (0.051 cm) from the edge of the mirror and the limiting ray of the return sample beam closest to the folding mirror will have a clearance of 0.020 inch (0.051 cm) minimum from the edge of the folding mirror. By setting the tolding mirror at 6.250 inches (15.875 cm) from the vertex of the primary mirror, the above clearance can be just achieved. The footprints of the outgoing laser beam and the return sample beam on the folding mirror for the folding mirror at this position are presented in Figure 7. These footprints are obtained at the expense of having an even smaller unused area at the center of the folding mirror. To avoid vignetting of the reference beam by the hole

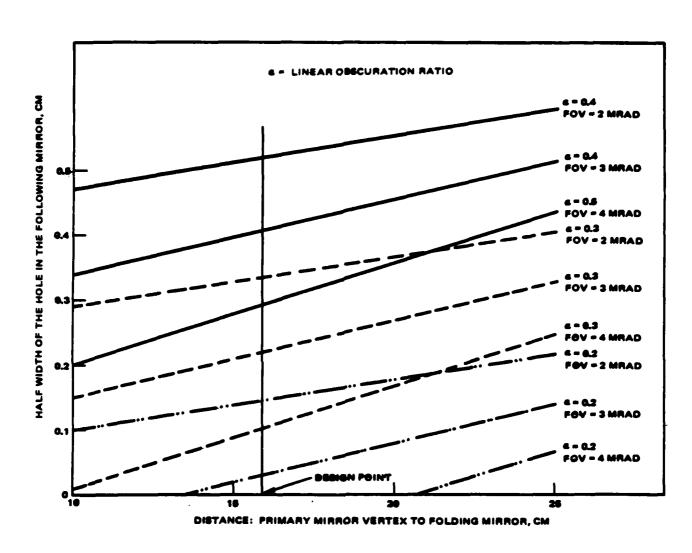


Figure 9. Inner ray clearance tradeoff at fold mirror.

in the folding mirror, the limit ray of the reference beam also had a clearance of 0.020 inch (0.051 cm) from the edge of the hole at the center of the folding mirror. The hole was set at 0.197 inch (0.5 cm) across the X-axis (Figure 7) so that at least a reference beam of 0.197 inch (0.5 cm) diameter would be allowed at the vertex of the primary mirror without vignetting for the full FOV. Consequently, the incoming laser beam at the folding mirror will be slightly vignetted by the hole at the folding mirror (shaded area in Figure 7) for field angles greater than 1.5 mrad. The maximum vignetting factor at the extreme field point would be 0.53 percent of the incoming laser beam cross section assuming an 0.3 obscuration ratio and 2 mrad maximum field angle. A small additional centroid shift could result for the return sample beam, but it can be avoided by increasing the obscuration ratio to 0.375 (as can be simulated readily by a mask appropriately placed in the beam path).

2.1.3 Optical Analysis

The HOLAB optical analyses included: (1) sample beam wavefront OPD map, (2) LOS accuracy, (3) output laser beam focusing range effects on LOS accuracy, and (3) optical tolerance sensitivity and alignment adjustments. These topics are described next.

Sample Beam Wave Front OPD Map. The sample beam optics together with the limit ray paths are presented in Figure 4. The OPD curves in the tangential and sagittal planes are shown in Figure 10 at three different field angles for both the sample beam and the outgoing laser beam. The outgoing laser beam wavefronts exhibit typical field curvature aberration, whereas the sample beam wavefronts have field curvature and residual comatic aberrations. The maximum wavefront deviation of the sample beam focus from that of the outgoing laser beam is about 0.35 wave peak-to-valley at 0.63 µm. The wavefront contour maps of the sample beam and the outgoing laser beam at the same three field angles is shown in Figure 11. These predicted wavefront contours are similar to the fringe pattern that might be seen in an interferogram.

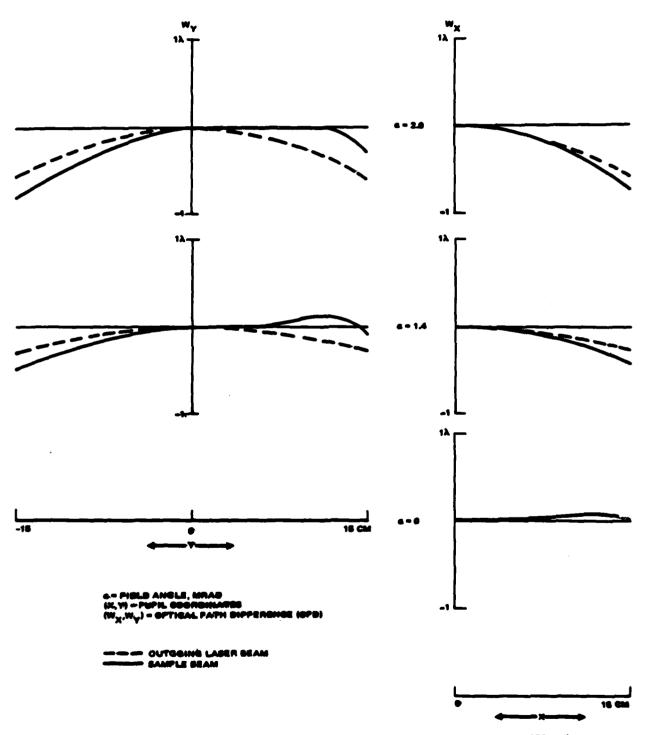


Figure 10. Wave front aberration for the outgoing laser beam and the sample beam (λ = 0.8328 μ m).

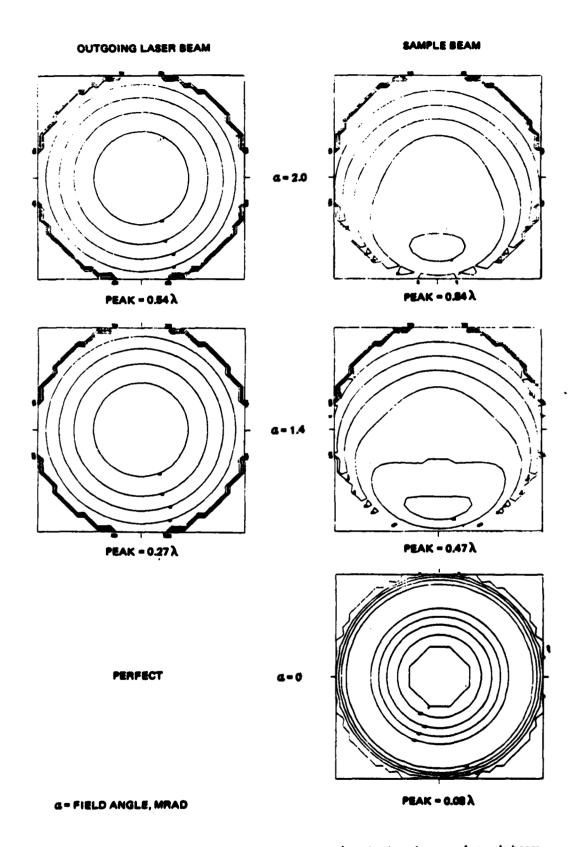


Figure 11. Wave front contour comparison between outgoing laser beam and sample beam.

LOS Accuracy. At an on-axis field angle, the reference beam and the sample beam are both focused to the same point near the vertex of the secondary mirror, and the centroids of both beams will be controlled to be coincident on the centroid detector. At the full field angle, the focal length of the vertex lens was adjusted so that the centroid of the reference beam coincides with that of the sample beam on the centroid detector. In this case, the centroid shift of the sample beam, for all practical purposes, is a linear function of the field angle. Consequently, the centroid difference between the sample beam and the reference beam is well within the LOS accuracy requirement (1 µrad) for all field angles. The LOS accuracy evaluation for the nominal system is shown in Table 2. The maximum predicted centroid difference between the reference beam and the sample beam is about 0.5 µrad in the detector space, which corresponds to 0.06 µrad in LOS accuracy.

Output Laser Beam Focusing Range Effects on LOS Accuracy. By adjusting the spacing between the confocal parabolas, the outgoing laser beam focusing range can be adjusted. As this separation is increased, the outgoing laser beam will be focused at a finite distance. The range effects on LOS accuracy are given in Table 3. The LOS error would be under 1 µrad if the outgoing laser beam is focused at a range greater than 1 km, which corresponds to a change in the separation between the confocal parabolas of less than 0.008 inch.

Optical Tolerance Sensitivity and Tolerance Compensating Adjustments. Manufacturing and alignment optical errors can easily cause the sample beam wavefront to deviate from that of the outgoing laser beam wavefront by more than one wave at 0.6328 micron. Spherical, comatic, and defocusing sample beam wavefront aberrations are introduced. The optical tolerance sensitivities of those breadboard optical element fabrication and alignment parameters that can effect aberrations in the sample beam are given in Tables 4 and 5. The change in the parameters are set according to standard optical industry practice. Adjustments are necessary to compensate the aberrations generated. First, the focal length of the primary

TABLE 2. LOS ACCURACY EVALUATION

FOV, mrad	Sample Beam Centroid mrad (in sensor space)	Reference Beam Centroid mrad (in sensor space)	LOS Accuracy, µrad
0	0	0	0
0.7959	6.3678	6.3673	0.06
1.3928	11, 1443	11.1438	0.06
1.9897	15.9219	15.9220	0.01

TABLE 3. CONFOCAL PARABOLA SEPARATION AND LOS ACCURACY

Increase in Confocal Parabola Separation, inch	Outgoing Laser Beam Focusing Range, km	LOS Change at 2 mrad Field Angle, µrad	
0	0.	0	
0.005	1.62	0.6μ	
0.010	0.81	1.2μ	

TABLE 4. SAMPLE BEAM COLLIMATING OPTICS MANUFACTURING SENSITIVITIES

		Change	Sample Beam Wavefront Aberration (λ = 0.6328 μ m)		
Parameter	Nominal Value		Comatic(\(\lambda\)	Spherical()	Focus Adjustment
Lens IV	4.190 in.	±0.004 in.		0.02	0.000 in.
Radii	12.615 in.	±0.013 ip.		0.02	0.000 in.
Lens V	1.516	±0.002 in.		0.02	0.001 in.
Radii	1.219	±0.001 in.		0.02	0.001 in.
Lens VI	5.834 in.	±0.006 ip.		0.02	0.001 in.
Radii	2.301	±0.002 in.		0.07	0.001 in.
Lens VII	9.586	±0.010 in.		0. 15	0.000 in.
Radii	3.512	±0.004 in.		0. 15	0.001 in.
Lens IV Thickness	0.235 in.	±0.002 in.		0.01	0.002 in.
Lens V Thickness	0.392 in.	±0.002 in.		0.25	0.003 in.
Lens VI Thickness	0.396 in.	±0.002 in.		0.20	0.001 in.
Lens VII Thickness	0.395 in.	±0.002 in.		0.04	0.000 in.
Lens IV Wedge	0	0.5 mrad	0.10		0.
Lens V Wedge	0	0.5 mrad	0.28		o.
Lens VI Wedge	0	0.5 mrad	0.10		0.
Lens VII Wedge	0	0.5 mrad	0.33		0.

^{*}Focus adjustment is performed by moving the collimating lens group axially along the optical axis

TABLE 5. SAMPLE BEAM COLLIMATING OPTICS ALIGNMENT SENSITIVITIES

Parameter	Nominal Value	Change	Sample Beam Wavefront Aberration (λ = 0.6328 μ m)		
			Comatic(\lambda)	Spheric(\(\lambda\)	Focus Adjustment
Spacing: Lens V to Lens VI	0.008 in.	±0.001 in.		0.12	0.001 in.
Spacing: Lens VI to Lens VII	0.008 in.	±0.001 in.		0.06	0.001 in.
Lens IV Tilt	0	±0.5 mrad	0.21		0
Lens V Tilt	0	±0.5 mrad	0. 16	}	0
Lens VI Tilt	0	±0.5 mrad	0.24		0
Lens VII Tilt	0	±0.5 mrad	0. 17		0
Lens IV Decenter	0	±0.001 in.	0.14		0
Lens V Decenter	. 0	±0.001 in.	0.44		0
Lens VI Decenter	0	±0.001 in.	0.17		0
Lens VII Decenter	0	±0.001 in.	0.16		0
Lens IV Index	1.525	±0.001 in.		0.08	.0.000 in.
Lens V Index	1.625	±0.001 in.		0.01	0.000 in.
Lens VI Index	1.625	±0.001 in.		0.04	0.001 in.
Lens VII Index	1. 625	±0.001 in.		0.27	0.001 in.

^{*}Focus adjustment is performed by moving the collimating lens group axially along the optical axis

TABLE 6. COLLIMATING OPTICAL ADJUSTMENT SENSITIVITIES

		Sample Beam Wavefront Aberration Sensitivities (λ = 0.6328 μm)		_	
Parameter	Nominal Value	Comatic	Spherical	Focus Adjustment	
Decentering of Collimating Lens Group	o	0.58 λ/mil		0	
Spacing between Lens IV and V	0.374 in.		0. 13 λ /mil	0.001 in.	

Focus adjustment is performed by moving the collimating lens group axially along the optical axis

mirror can be measured and adjustments to the construction optics distances computed to take the actual mirror radius into account. Second, manufacturing and alignment errors can be compensated by making collimating lens adjustments (Figure 4). Focusing error can be deleted by adjusting the collimating lens group along its optical axis. A lateral adjustment of the collimating lens as a whole can compensate for the comatic aberration. By adjusting the spacing between the negative lens element and the three element positive lens group, the spherical aberration can be reduced. The collimating lens optical adjustment sensitivites are given in Table 6. Detailed tolerance analyses have concluded that with these three collimating lens optical adjustments and the assignment of the optical parameter tolerances according to standard optical industry practice, the sample beam wavefront can be adjusted to that of the nominal design. The three alignment adjustment ranges required are presented in Table 7 and must be accommodated by the mechanical design.

The reference beam optics is an extremely slow system of F/70. The optical errors produced by standard optical practices can be tolerated by lateral and axial adjustments of the vertex lens pair as a whole and the spacing between the lens pair. Tolerances for the vertex lens are given in Table 8.

TABLE 7. COLLIMATING LENS OPTICAL ADJUSTMENT RANGES REQUIRED

Nominal Value	Adjustment Range, mils
0.663 in.	±47
0	±30
0.374 in.	±20
	Value 0.663 in. 0

TABLE 8. VERTEX LENS TOLERANCE

Parameter	Nominal Value	Tolerance*
Lens VIII	37. 900 in.	±0.038 in.
Radii	3.660 in.	. ±0.004 in.
Lens IX	34.473 in.	±0.034 in.
Radii	3.015 in.	±0.003 in.
Lens VIII Thickness	0.203 in.	±0.002 in.
Lens IX Thickness	0.203 in.	±0.002 in.
Lens VIII Wedge	0	±0.6 mrad
Lens IX Wedge	0	±0.6 mrad
Lens VIII Tilt	0	±1.5 mrad
Lens IX Tilt	0	±1.5 mrad
Lens VIII Decenter	0	±0.001 in.
Lens IX Decenter	o	±0.001 in.

^{*}Negligible performance degradation results from these values because of the slow (F/70) lens speed.

2.1.4 Breadboard Component Descriptions

The major optical components of the HOLAB breadboard and their fabrication tolerances and dimensions are detailed in this section.

Beam Expander. The optical specification of the HOLAB f/1.5 confocal parabolic primary and secondary mirrors required that the wavefront emerging from the combination should not be irregular by more than $\lambda/2$ ($\lambda = 0.6328 \ \mu m$) when a plane wavefront is incident on the secondary mirror. The beam expander is shown in Figure 12.

Reference Flat Mirror. The optical specifications of the reference flat used to retroreflect the outgoing beam require that the flat be polished to a radius of infinity $\pm \lambda/2$ and to an irregularity not greater than $\lambda/8$ ($\lambda = 0.6328 \mu m$). The reference flat is shown in Figure 13.

Beamsplitters and Mirrors. The diameters of the beamsplitters and mirrors (excluding steering mirrors SM1, SM2 and SM3) were specified as 4.0 inches (0.500 inch thick) to enable standard catalogue items to be used to mount these components.

The diameter of the steering mirrors was specified as 3.0 inches (0.500 inch thick) to enable the steering inertia to be comfortably below the 1000 gm-cm² limit imposed by the selection of G-300 PDT scanners. The reduced diameter of the steering mirrors is accommodated by mounting SM1 and SM2 at 30 degrees to the incident test beam laser (all other components are mounted at 45 degrees) and by positioning SM3 near the location of the primary mirror image formed by the collimating lens.

The substrates for these components were specified to have a polished surface flatness of $\lambda/20$ ($\lambda=0.6328~\mu m$) within a 80 percent clear aperture for the 4.0 inch diameter components and within a 90 percent clear aperture for the 3.0 inch diameter components. Both surfaces of the beamsplitters were specified for a flatness of $\lambda/20$. All folding mirrors were coated with a high reflectivity (R > 99.8 percent at $\lambda = 0.6328~\mu m$) dielectric coating for use at angles of incidence of 30 and 45 degrees. The folding mirror is shown in Figure 14.

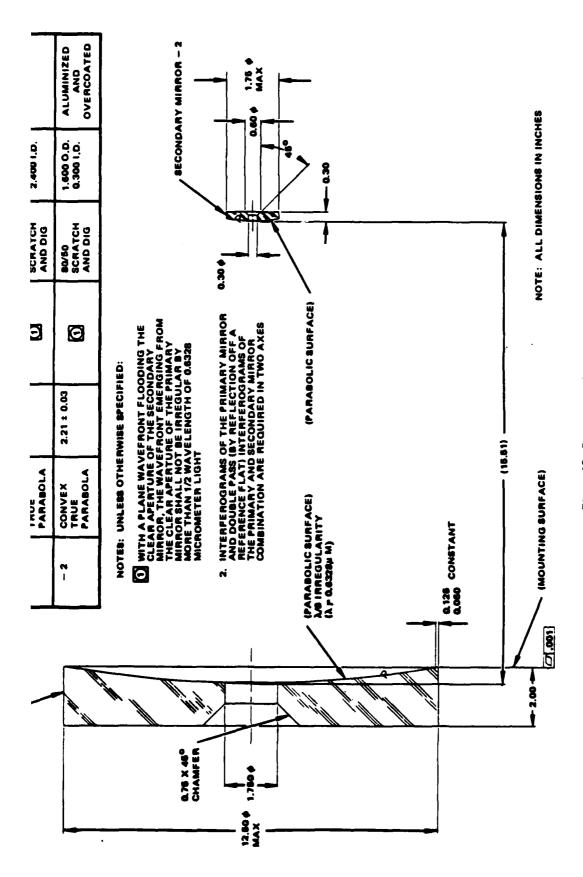
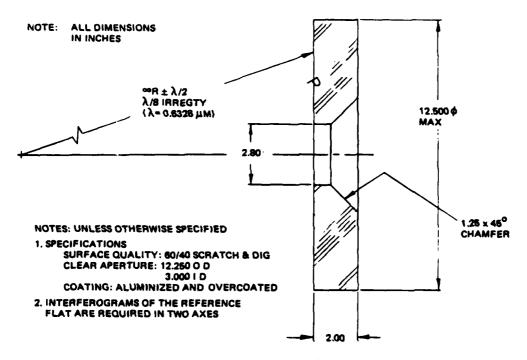


Figure 12. Beam expander.

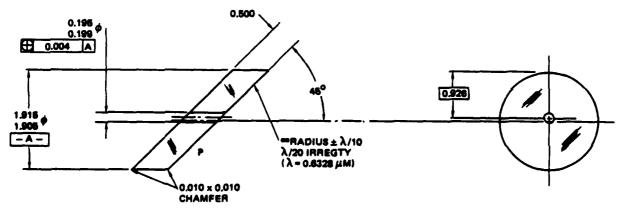


Г

Г

ŗ

Figure 13. Mirror, reference flat.



NOTES: UNLESS OTHERWISE SPECIFIED

1. SPECIFICATIONS:

SURFACE QUALITY: 60-40 SCRATCH & DIG CLEAR APERTURE: WITHIN 0.020 OF OUTSIDE EDGE AND WITHIN 0.020 OF INNER HOLE, COATING: ALUMINIZE & OVERCOAT

2. Surface Marked "7" Polished, all other surfaces ground

Figure 14. Folding flat mirror.

2.1.5 Breadboard Radiometry

Beamsplitters are required to separate a portion of the test laser beam for use as an interferometric reference, and to combine the sample beam, outgoing beam and reference beam along the same optical path for interferometry. The required beam splitting ratios of the beamsplitters were calculated. This calculation considered the reflectivity of mirrors, the diffraction efficiency of the holographic grating, the input laser power, and the energy density required to record interference fringes on film. The anticipated reflectance or transmittance values for each optical component in the HOLAB breadboard is given in Table 9.

The reflectances and transmittances of the beamsplitters that will equalize the energy in the sample, outgoing and interferometric reference beam are given in Table 10. Two of the beamsplitters have beamsplitting coatings on the front surface (BS3 and B4); two of the beamsplitters use the energy reflected at the air-glass interface to achieve the proper beamsplitting ratio (BS1 and BS2). Each parallel plate beamsplitter has an antireflection coating on the back surface to reflect less than 0.1 percent of the incident light. The beams reflected at the second surface, therefore, will be reduced in magnitude, with respect to the front surface reflected beam, by (0.001) x (transmittance of the beamsplitter)² and will at the worst case, (uncoated beamsplitter BS1 and BS2) be less than 0.9 percent of the front surface reflection. The effect of this light on the contrast of the desired interference fringes formed between the outgoing or sample beam and the interferometric reference beam is negligible.

Polarization Dependent Effects. The polarization dependent effects of the optical components that comprise the HOLAB Breadboard were determined and are detailed below. This determination was made because the output of the test beam laser is linearly polarized.

- 1. The high reflection coating on the beam direction, translation, and steering mirrors and the folding flat reflect greater than 99.8 percent for both s and p polarized light.
- 2. The beamsplitting coating on the front surface of the parallel plate beamsplitters must be specified for s or p polarization.

TABLE 9. REFLECTANCE AND TRANSMITTANCE OF HOLAB OPTICAL COMPONENTS

Components Common to All Beams		
Beam Directing Mirror 1	0.998	
Beam Directing Mirror 2	0. 998	
Pockels Cell	0.76	
Beam Expander (without pinhole)	0. 94	
Pinhole (in beam expander)	0. 993	

Components Specific to Each Beam							
Refe	rometric rence am	Outgoing Be	am	Sample Bear	n.	Reference Bes	ım
BS2 R	0.0921	BS2 T	0. 9079	BS2 T	0.9079	Periscope	0. 996
Ml	0.998	BSI T	0. 9079	BS1 T	0. 9079	Corner Cube	0. 95
M2	0.998	BTM	0. 998	ВТМ	0.998	Vertex Lens	Q. 9 Q
мз	0.998	SMI	0. 998	SM1	0.998	Collimating Lens	0. 95
BS3 R	0. 27	SM2	0. 998	SM2	0.998	SM3	0.~998
		Folding Flat	0. 998	Folding Flat	0.998	B\$4	0.500
		Secondary	0. 89	Secondary	0.89	Detector Lens	0. 90
		*Primary	0.76	*Grating	0. 10		
		Reference Flat	0.89	Collimating Lens	0. 95		
		*Primary	0. 76	SM3	0. 998	ļ	
		Secondary	0. 89	BS1 T	0.9079		
		Folding Flat	0. 998	BS4 T	0.500		
		SIM2	0. 998	BS3 T	0.7289	\	
		SM1	0. 998	ļ		l .	
		BTM	0.998			ii	
		BS1 R	0.0921				
		BS3 R	0.7289				

^{*}Assuming a holographic diffraction grating efficiency of 0.10.

TABLE 10. BEAMSPLITTING RATIOS FOR HOLAB COMPONENTS

	Calculated	Anticipated
BSI	0.9079 T	0.9079 T
	0.0921 R	0.0921 R
BS2	0.9079 T	0.9079 T
	0.0921 R	0.0921 R
BS3	0.2711 T	$0.3000 \pm 5\% T$
	0.7289 R	$0.7000 \mp 5\% R$
BS4	0.5000 T	$0.5000 \pm 5\% T$
	0.5000 R	0.5000 ∓5% R

- 3. The reflection coefficient at an air/glass (n = 1.50) interface for an angle of incidence of 45 degrees is 0.0921 for s polarized light and 0.0085 for p polarized light. Parallel plates with uncoated front surfaces could be used as beamsplitters when the desired reflectance from the surface matches the reflection coefficient of the uncoated surface.
- 4. Antireflection coating on beamsplitters will reflect less than 0.1 percent of both s and p polarized light.
- 5. The holographic grating is polarization sensitive. Greater uniformity is obtained for the p polarization as a function of positional radial. Nonuniformities occur in the s polarization when a diffraction order begins to radiate. In spite of these effects, the overall beam profile appears to be sufficiently uniform. Therefore, for low efficiency gratings, the groove depth or profile of the grating across should not have to be tailored as a function of radius for either polarization.
- 6. Problems that could arise because of phase shifts existing between reflected beams with s and p polarization are assumed negligible because the input beam is linearly polarized.
- 7. The diffraction efficiency of the grating will vary as a function of angular orientation because the linearly polarized test beam laser changes from parallel to perpendicular to the grooves of the circularly symmetric holographic diffraction grating every 90 degrees.

Because the diffraction efficiency of the s and p polarizations are only slightly different and because the efficiency of the holographic grating is low, items 5 and 7, above, were not expected to affect the performance of the HOLAB experiments.

Interferometer Film Selection. Polaroid film type 57, ASA 3000, was selected to record interferograms. The exposure required to produce a visual density of 0.5 (a density just noticeably darker than white) on this positive film (greater exposure, less density) is approximately 0.005 ergs/cm². The average energy density on the film was calculated to be 5.2 ergs/cm²-sec. Thus, a film exposure of a fraction of a second on Polaroid film type 57, ASA 3000, is required.

2.2 MECHANICAL DESIGN

2.2.1 Introduction

The mechanical design task consists of the layout, design, procurement, and fabrication of the mechanical components associated with the HOLAB breadboard. The breadboard design incorporates a commercially available optical table complete with isolation supports. The secondary mirror is provided with three orthogonal axes of translation. One axis, manual, off-axis steering of the output beam from the beam expander of ±2 mrad is also included. Provisions to distort the primary mirror substrate are built into its support. Adjustments are provided where appropriate for proper operation and ease of assembly of the breadboard.

2.2.2 General Layout

As shown in an early perspective view of the overall breadboard (Figure 15), standard laboratory optical mounts have been incorporated wherever possible throughout the assembly. Adjustments to the optical components are easily accessible because of their location on the isolated table. These components are described in more detail in this subsection.

2.2.3 Component Design Features

Optical Table. The optical table, with its isolation supports, was procured from Newport Research Corporation. The table (RS410-18) is 4 feet by 10 feet, and 18 inches thick. It has a 3/16 inch thick ferromagnetic stainless steel top skin with 1/4-20 mounting holes on 1-inch centers. It also has a high density steel honeycomb core and an internal damping system to suppress structural resonances. The four supports (XL4A-16) are 16 inches

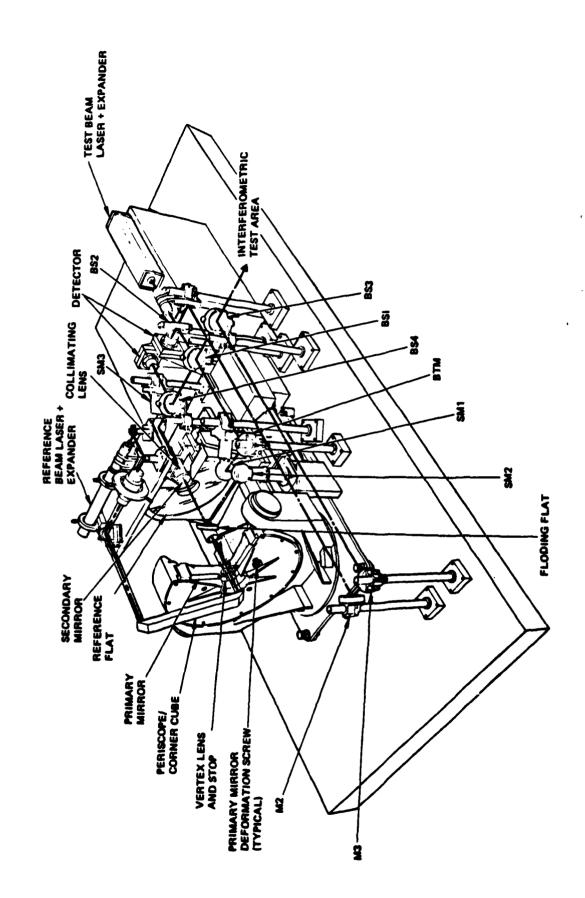


Figure 15. HOLAB breadboard.

high. These free standing pneumatic isolation mounts have pneumatic height sensing control valves.

Primary Mirror. The primary mirror is assembled into a type YMM-16C mount, supplied by the John Unertl Optical Company (Figure 16). This mount is designed to accept a 16-inch diameter mirror. The Hughes 12.5 inch diameter mirror mounts into an adapter cell to fit the exiting 16-inch diameter. Independent angular adjustments in both planes are made by handwheel driven precision screws that operate in a push-pull manner. The center of rotation of either angular motion is coincident with the apex of the primary mirror.

The primary mirror can be deformed by using a special thumb screw threaded through the rear cover of the primary mirror mount (Figure 17). These screws may be placed at various chosen positions to achieve different deflection patterns on the mirror.

Up to 100 pounds of force may be applied to the back surface of the mirror with a nylon tipped plunger. A controllable force is provided by the compression of five Belleville spring washers that are stacked in series and held together by a shim and retaining ring. The force magnitude is monitored by slowly turning the screw clockwise and measuring the amount of plunger movement with a caliper from the top of the thumb screw to the top of the plunger. This measurement will indicate how much force is actually pushing on the mirror (2 pounds per 0.001 inch). This amount may be calibrated before assembly by use of a force gauge and a caliper.

The NASTRAN structural analysis program was used to predict analytically the surface deformation characteristics of the HOLAB primary mirror that result from a variety of static loading conditions. The mirror was assumed to be in a three-point kinematic edge mount for the following loading conditions:

- 1. One G LOS (line of sight) gravity load only (Figure 18)
- 2. Various combinations of localized LOS forces (Figures 19 through 29) with no gravity loads.

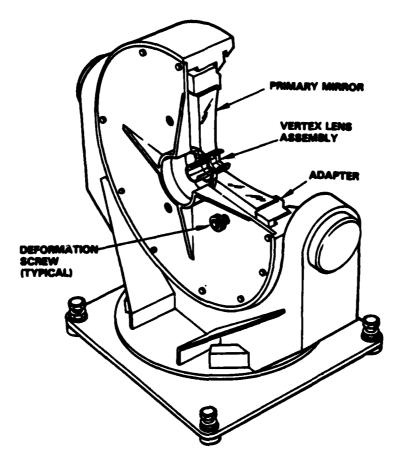


Figure 16. Primary mirror mount.

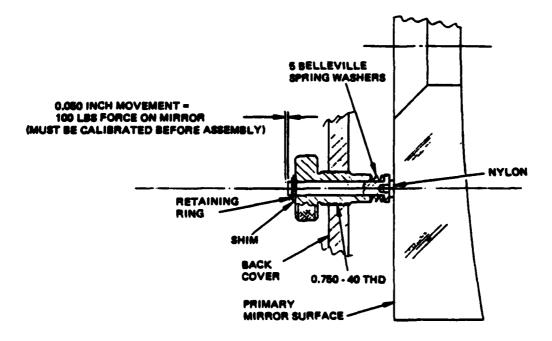


Figure 17. Primary mirror deformation device.

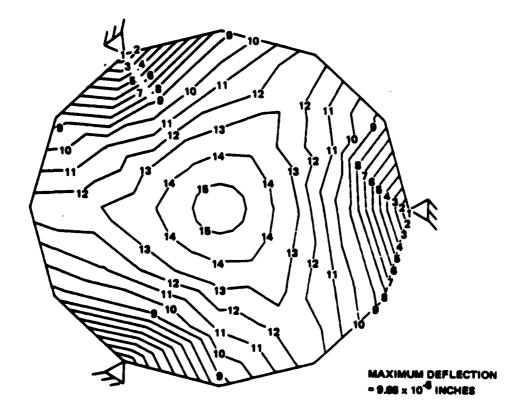


Figure 18. Ig LOS gravity load.

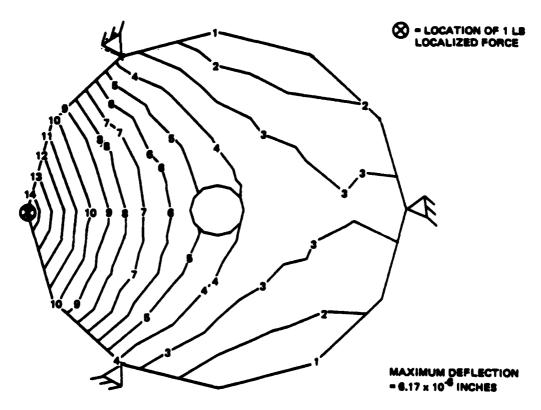


Figure 19. Single-point edge loading.

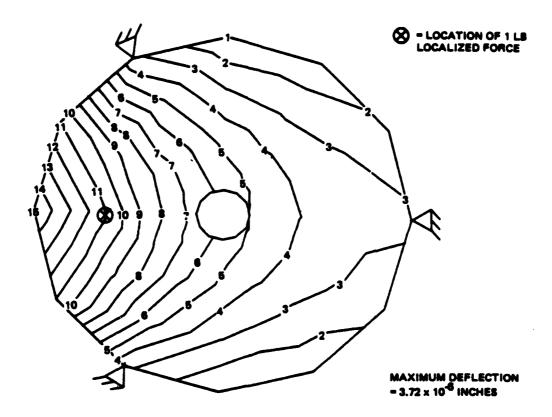


Figure 20. Single-point intermediate loading, Case A.

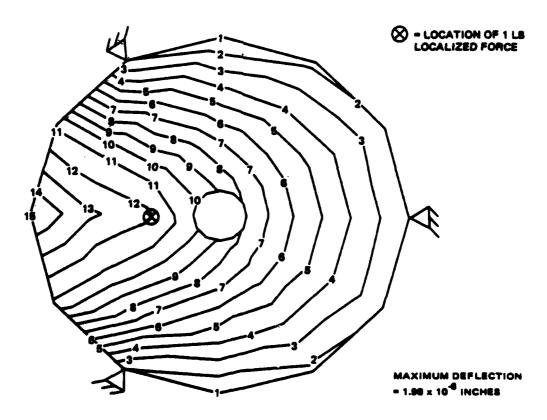


Figure 21. Single-point intermediate loading, Case B.

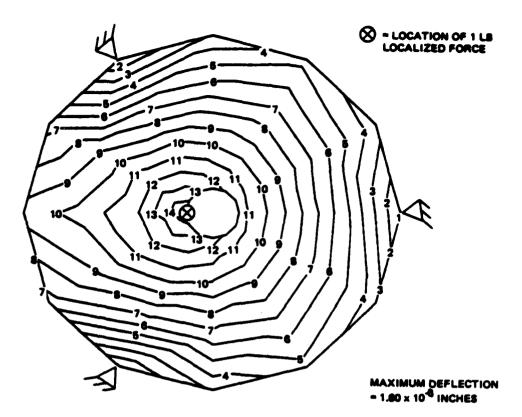


Figure 22. Single-point intermediate loading, Case C.

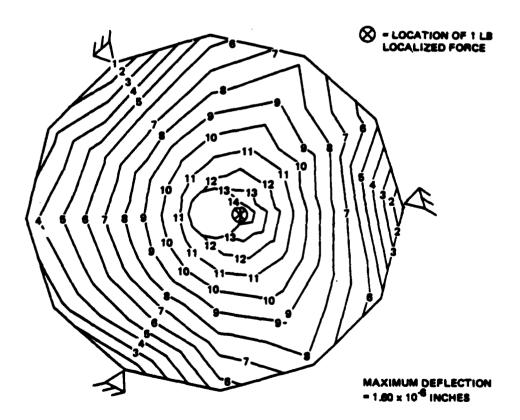


Figure 23. Single-point intermediate loading, Case D.

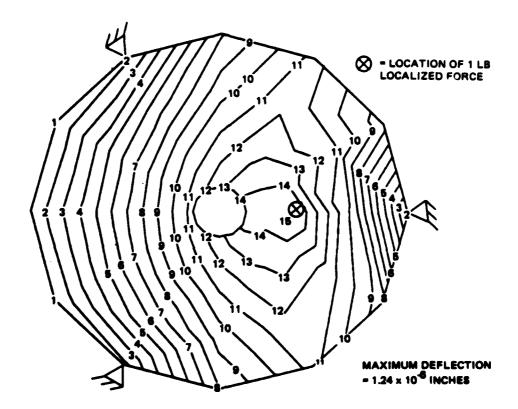


Figure 24. Single-point intermediate loading, Case E.

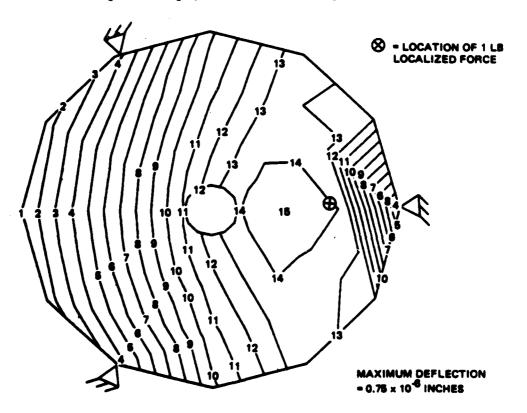


Figure 25. Single-point intermediate loading, Case F.

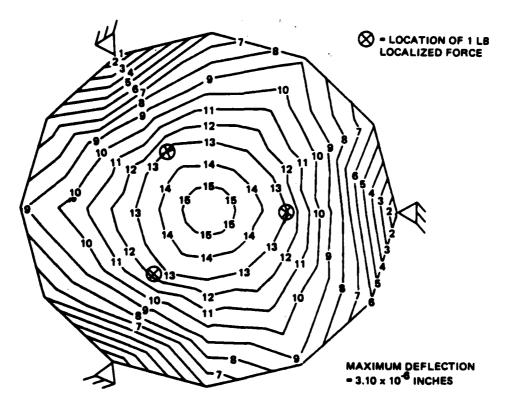


Figure 26. Three-point loading.

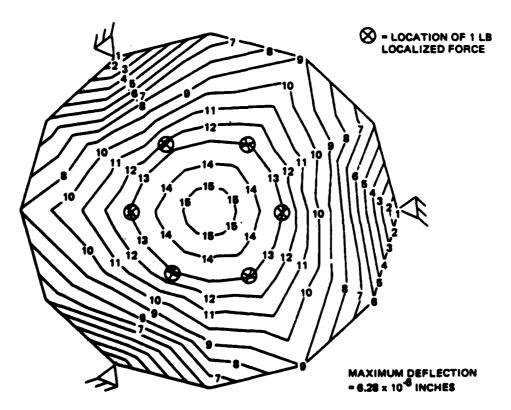


Figure 27. Six-point loading.

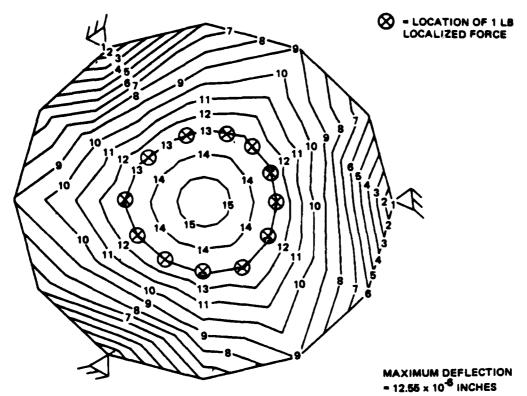


Figure 28. Twelve-point loading.

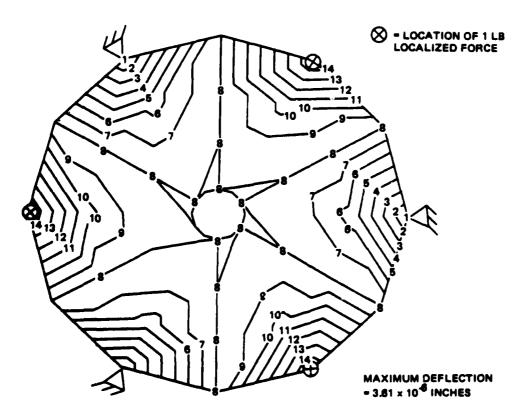


Figure 29. Three-point edge loading.

Fach adjacent contour on the computer drawn illustrations represents a change of 1/15 of the maximum surface deflection. For a localized force of X pounds, a maximum deflection of X times the states maximum deflection can be assumed. Hence, to achieve a surface deflection of 100 microinches (four waves at 0.6328 μ m) with a localized force located as illustrated in Figure 21 would require:

$$\frac{100 \times 10^{-6}}{1.98 \times 10^{-6}} = 50 \text{ pounds of force}$$

The vertex lens assembly is bonded to the back surface of the primary mirror and protrudes through a hole in the center of same (Figure 16). The entire assembly is adjustable radially ± 0.020 inch and axially ± 0.060 inch. The airspace between the two lens elements is adjustable ± 0.060 inch.

Reference Flat. The reference flat mirror has been assembled in a mirror mount procured from Daedal, Incorporated (Customized Model 2355). It has a two-axis kinematic pivot adjustment with three-point orthogonal suspension. Off-axis steering of the output beam from the beam expander is accomplished by one-axis rotation of the reference beam laser, which is mounted on top of the reference flat mount and moves in unison with it (Figures 30 and 31).

Collimating Lens Assembly. The collimating lens assembly consists of four lens elements mounted in the same cell (Figure 32). The elements are held in place by threaded retainers and separated by spacers.

The collimating lens assembly and steering mirror 3 (SM3) are mounted on the same bracket that is mounted to NRC translation stages (Figure 33). The steering mirror 3 (SM3) pivot axis is located at an image of the primary mirror. The collimating lens can be adjusted in translation in three orthogonal directions.

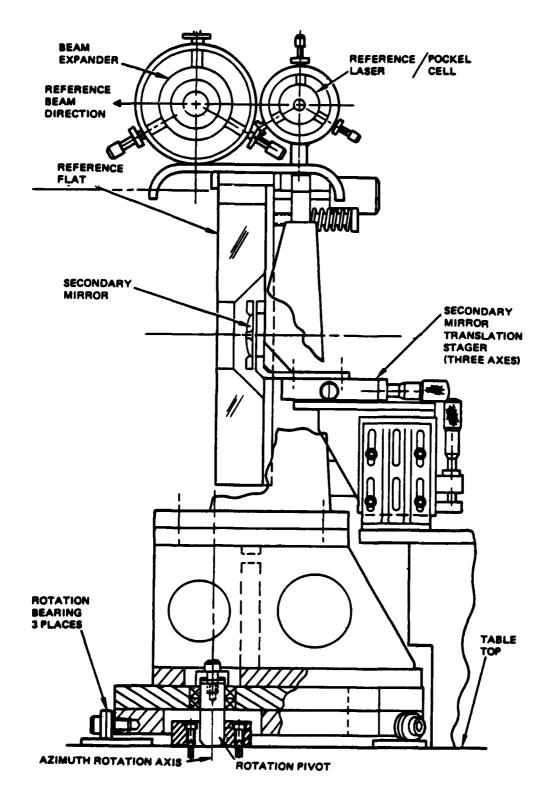


Figure 30. Reference beam laser mounted on reference flat (side view).

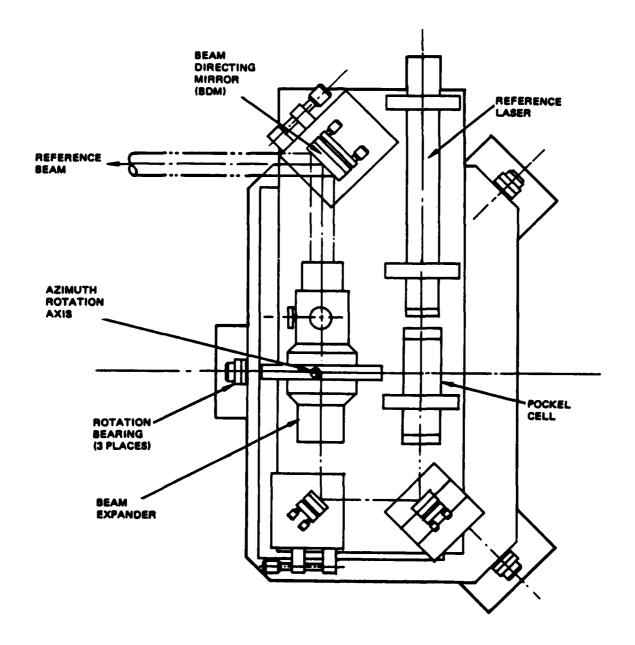


Figure 31. Reference beam laser mounted on reference flat (top view).

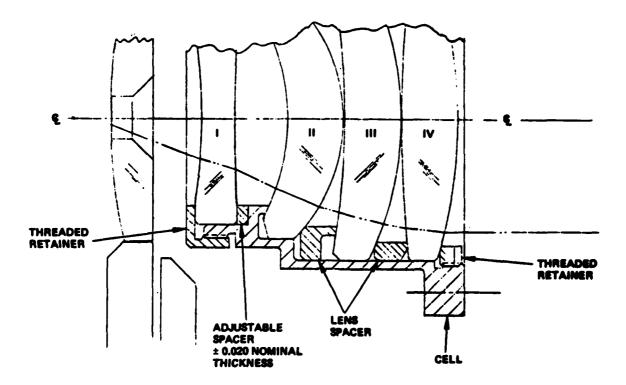


Figure 32. Collimating lens assembly.

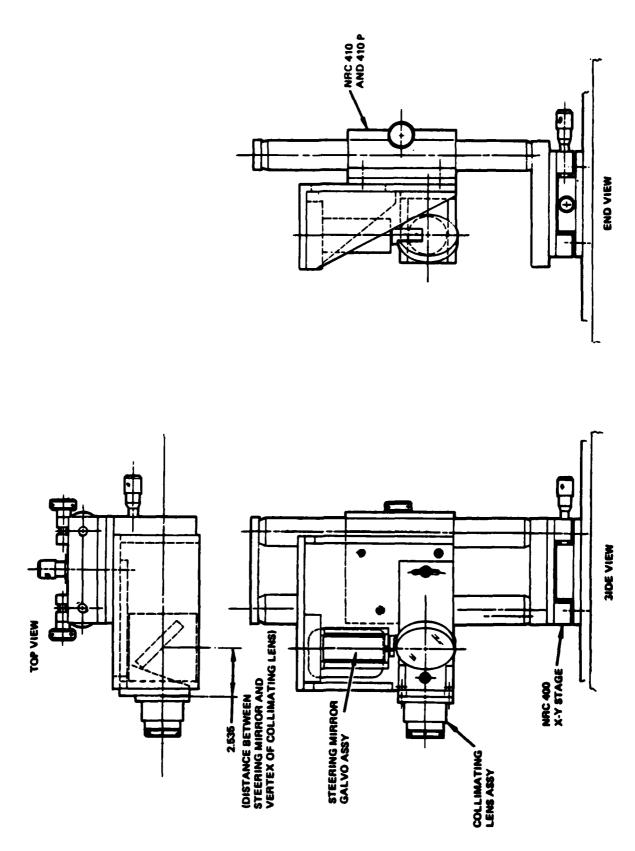
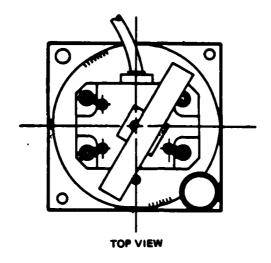


Figure 33. Collimating lens/steering mirror 3 assembly.

Steering Mirror/Galvo Assembly. The three scanners are each assembled on a Hughes-designed mount. These mounts attach to an NRC (RSX-2) rotational stage (Figure 34). The steering mirrors are cemented to a Hughes-supplied mounting bracket that is secured to the scanner shaft by two setscrews.

<u>Detector Assembly</u>. The sample beam detector and outgoing beam detector are both to be mounted on separate Hughes-supplied boxes and both adapted to an X, Y, Z translation stage from NRC (Figure 35). The detector lenses with a focal length of 31.25 cm and appropriate lens cell were procured from Klinger Scientific.



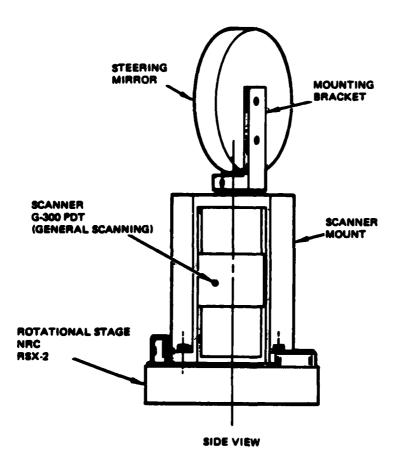


Figure 34. Steering mirror/galvo assembly.

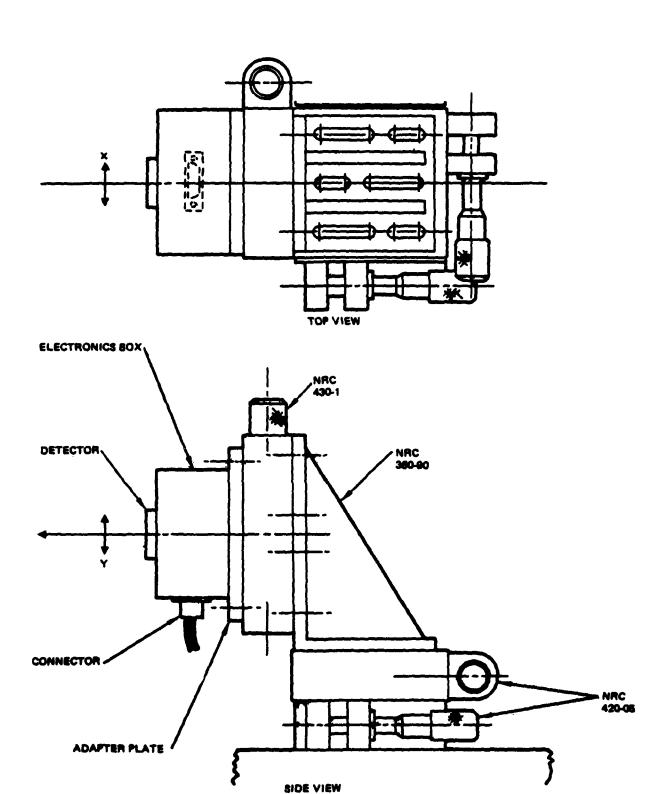


Figure 35. Detector mount.

2.3 SERVO AND CONTROLS DESIGN

2.3.1 Introduction

The objective of the servo and controls effort has been the design, fabrication, procurement, and integration of the system servo and sensor electronics. Two axis, closed loop, automatic alignment of the sample beam with respect to the reference laser beam and closed loop, automatic alignment in azimuth of the reference laser beam has been provided.

The servo and controls effort is discussed for three major areas: laser sources, steering mirrors, and angle sensors.

2.3.2 Laser Sources

The HeNe laser sources are considered to be composed of pockel electro-optic modulators, laser collimators with spatial filters, and the lasers themselves. The first and most important is the laser itself. In the selection of the reference and test lasers, several characteristics were considered desirable. These included output power, stability, size, and degree and type of polarization. Size was a critical parameter for the reference laser because of its location atop the reference flat. The test laser required a higher output power than the reference laser because of greater optical transmission losses in its path. Linearly polarized laser light was required for both the test and reference lasers to facilitate operation of the Pickels' electro-optic modulator. The lasers chosen met the specifications given below:

1. Test Laser (Spectra Physics 120)

a.	Wavelength:	632.8 nm
b. Output Power: 5 mW		5 mW
c.	Polarization:	Linear, 1000:1
d.	Dimensions:	470 x 83 x 80 mm (1 x w x h)
e.	Output Beam Diameter:	0. 79 mm at 1/e ² points
f.	Long Term Power Drift:	<5 percent

2. Reference Laser (Spectra Physics 145P)

a. Wavelength: 632.8 nm

b. Output Power: 1.5 mW

c. Polarization: Linear, 500:1

d. Dimensions: 35 mm dia x 286 mm

e. Output Beam Diameter: 0.5 mm at 1/e² points

f. Power Drift: ±1.5 percent in 12 hours

The second element in the laser source is the Pockels' electro-optic modulator. The Pockels' electro-optic effect describes the phase changes produced in polarized light passing through certain uniaxial crystal materials, which are under the stress of an electric field. The effect of a Pockels' electro-optic modulator (EOM) on polarized light is similar to the effect obtained with optical retarders such as 1/4 or 1/2 wave retardation plates. A retardation plate, operating with light of a given wavelength, introduces a fixed phase shift between the ordinary and extraordinary light rays passing through the plate. The electric vectors of the light experience a rotation, which is determined by the thickness of the plate and the birefringence of the material. In an EOM, the value of the birefringence is controlled electronically to produce a desired optical retardation. The three characteristics that determined the selection of the particularly EOM were physical size, quarter wave voltage, and linear aperture. In addition, a large linear aperture is desirable for ease of alignment. However, a large aperture requires an undesirably large quarter wave voltage. Also, the length of the modulator is inversely proportional to drive voltage. Hence a tradeoff was made between length, voltage, and aperture size. An EOM of low voltage and moderate length and aperture size was chosen. The modulators selected, Pockels' Electro-Optic Modulator (Lasermetrics 3079F), met the following specifications:

1. Linear Aperture: 2,25 mm

2. Extinction Ratio: 500:1

3. Quarter Wave Voltage: 100 volts at 632.8 nm

4. Dimensions: 40.6 mm dia. x 127 mm long

The third and fourth elements of the laser sources, the spatial filter and laser collimator, were combined because of the selection made. The spatial filter is required to eliminate the unwanted intensity fluctuations across the beam profile. These fluctuations are caused by interference effects from light scattered by dust particles in the air and on the mirrors and lenses and from lens defects. Focusing the laser light onto the focal plane of a positive lens forms the optical power spectrum of the light distribution. Usually the higher frequency noise spectrum is separated from the focused Gaussian; therefore, the unwanted light can be blocked and desired Gaussian passed with a spatial filter. The pinhole spatial filters required for the two laser collimators were determined in the following manner. The diffraction limited spot size of a Gaussian beam truncated at its $1/e^2$ points is

$$D = 1.83 \frac{\lambda d}{f}$$

for

 $\lambda = 632.8 \text{ nm}$

f = 3 mm (280-XX-075 entrance lens)

d = 0.75 mm

 $D = 4.63 \times 10^{-6} \text{ m}$

A pinhole that would pass a beam of at least twice this diameter is desirable. A 10 μ m spatial filter was selected for both the reference and test beams.

Requirements for the selection of the laser collimator included proper magnification ratio, builtin spatial filter, and optical performance of $\lambda/8$ or better. The selected collimators had the following characteristics:

1. Test Laser Collimator (TROPEL 280-50-075)

a.	Magnification:	66.7X	
b.	Exit Aperture:	50 mm	
c.	Spatial Filter Pinhole:	10 μm	
đ	Ontical Performance) / Q	

2. Reference Laser Collimator (TROPEL 280-25-075)

a. Magnification: 33.3X
b. Exit Aperture: 25 mm
c. Spatial Filter Pinhole: 10 μm
d. Optical Performance: λ/8

To obtain a greater uniformity across the aperture of the test and reference beams, the output beam diameters from the beam expanders are larger than ultimately required. The predicted energy available to the outgoing beam detector, the sample beam detector, and the interferogram recording plane is given in Table 11. The alignment detectors require between 10 and 100 μ W for reliable operation.

2.3.3 Angle Sensors

The two HOLAB angle sensors each consist of focusing optics, a photopot position detector, and signal processing electronics.

Each focusing system consists of a lens element with an effective focal length of 31.25 cm. Viewed from beam expander output space, the effective focal length seen by the sensor is 2.5 meters. The collimated and modulated beams are focused on the photopot that measures beam position in the focal plane, which is related to angular input to the sensor by Δx f $\Delta \theta$,

TABLE 11. DETECTOR AND INTERFEROGRAM PLANE ENERGY LEVELS (IN µW)

	Beam D		
Beams	Outgoing	Sample	Interferogram Plane
Outgoing	47	-	42
Sample	-	44	42
Interferometric Reference	-	•	42
Reference	-	44	-

where Δx is focal plane displacement, f is the focal length and $\Delta \theta$ is the entrance angle. Beam position is insensitive to translations of the beam at the entrance aperture to a first order.

United Detector Technology model SC-10D dual axis position sensors are used as the detectors. They provide X and Y-axis position information of a light spot on the detector surface. These devices sense the centroid of the light spot and provide continuous analog output as the light spot moves from null point to the limit of the active area. Output current is proportional to the input beam position relative to each of the device's four terminals. The signal is then preamplified and transmitted to the processing electronics.

The preamplifier is a transconductance mode FET input operational amplifier that converts the current signal into a voltage signal. Then the signal is differentially sent to the signal processing electronics (Figure 36). The two signals present on detector 1 (Figure 37), the reference beam and the sample beam, can be separated electronically since they are modulated at two different, nonharmonic frequencies. The signal processing electronics converts modulated beam position data into voltages corresponding to beam position in orthogonal axes. These signals are used to control the three galvo steering mirrors.

The noise limited angular resolutions in output space for the two sensors are calculated below as noise equivalent angles (NEAs).

NEA =
$$\frac{\frac{E_N}{R_F}}{(Pos. Sens.)} \times \frac{\sqrt{BW}}{P_{INC} \times \frac{1}{\pi}} \times \frac{1}{EFL}$$
 (radians)

where:

$$E_{N} = 12 \text{ nV}/\sqrt{\text{Hz}} \text{ (preamp)}$$

$$R_{\rm F} = 100 \text{ K}\Omega$$

Pos. Sens. = 0.32 A/W-cm (position sensitivity)

$$BW = 60 Hz$$

$$EFL = 250 cm$$

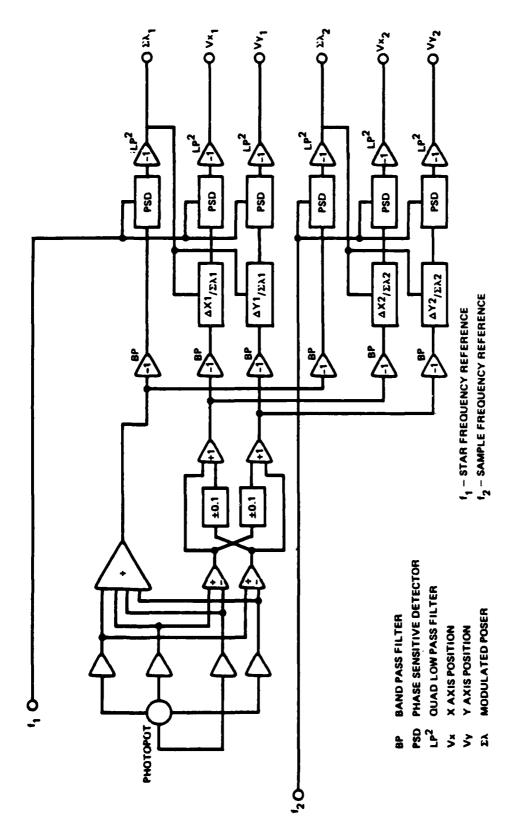


Figure 36. Angle sensor electronics.

J

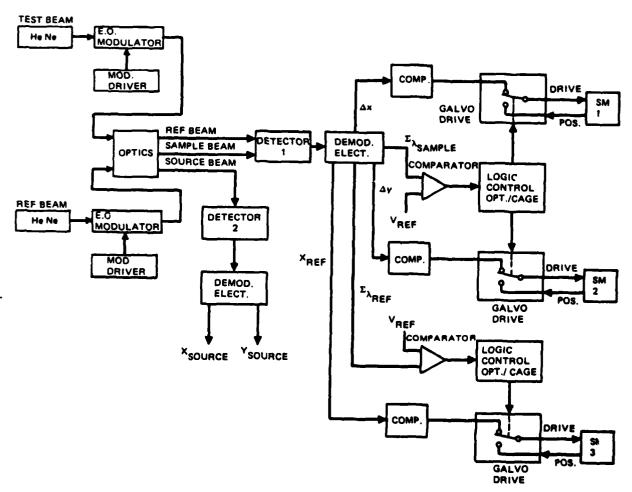


Figure 37. HQLAB electronics functional block diagram.

and the energy incident on the two detectors is:

 P_{INC} for sample beam = 44 μ W

 P_{INC} for reference beam = 44 μ W

 P_{INC} for outgoing beam = 47 μW

Therefore,

NEA (sample beam and reference beam) = 83 nrad in output space

NEA (outgoing beam) = 69 nrad in output space

The detectors are protected against 60 Hz room lighting by electronic filtering and a metal shroud over each detector.

The three galvanometer-drive, single axis, steering mirrors are controlled by three channels of error signal from the alignment detector signal processing (Figure 37). Steering mirror 1 is driven by the difference in X-axis position signals on detector 1 between the reference beam spot and the sample beam spot. Steering mirror 2 is driven similarly by the difference in Y-axis position signals on detector 1 between the reference and sample beams. Steering mirror 3 is driven by the X-axis position signal on detector 1 of the reference beam. The signal processing is such that the sample beam will track the reference beam. The signals from detector 2 do not drive any steering mirrors and are only used to verify the position of the retroreflected outgoing beam.

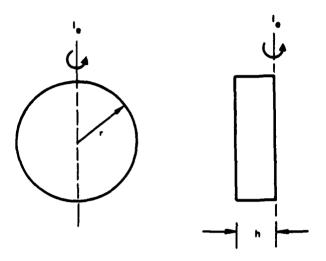
2.3.4 Steering Mirror

General Scanning G300PDT optical scanners and drive electronics were selected to perform the beam steering functions. These scanners are capable of position loop bandwidths of 5 to 10 Hz with large mirrors installed and have a position readout sensitivity of 1 second of arc. Their drive electronics were modified so that they could be integrated with the

detector signal processing. Scanner temperature regulation is controlled to better than 1/2°C, which provides control over zero drift and gain drift in the position loop mode.

The G-300 PDT scanners have a limit of 1000 gm-cm² of inertia. The inertia of the steering mirrors is given by:

$$I_e = \frac{m}{12} (3r^2 + 4h^2)$$



where:

$$r = 3.81 \text{ cm}$$

$$h = 7.62 \text{ cm/6} = 1.27 \text{ cm}$$

$$Density of mirror = 2.2 \text{ gm/cm}^3$$

$$m = (\pi)(r)^2(h) \text{ (density of mirror)} = 127.4 \text{ gm}$$

Therefore,

$$I_e = 530.8 \text{ gm-cm}^2$$

which is within the specifications of the scanner.

SECTION III HOLOGRAPHIC GRATING FABRICATION

3.1 INTRODUCTION

The grating is a shallow relief pattern, which is ion beam etched on the gold surface of the primary mirror through a holographically exposed photoresist mask. The grating pattern is a series of concentric grooves. The grating spatial frequency that increases radially across the mirror surface thereby provides on axis beam sampling with focusing power. Diffraction efficiency of the sampled beam is dependent on details within the grating structure such as grating depth and profile. These parameters are subject to the photoresist thickness, exposure energy, and ion beam etching. The wavefront of the sampled beam is dependent on the global accuracy and distribution of the grating spatial frequencies over the mirror surface. An aberration correcting construction optics design is used, and the holographic exposure system is meticulously aligned.

The fabrication of a holographic, beam sampling, surface grating on the HOLAB 30 cm diameter, F/1.5, parabolic primary mirror consisted of four subtasks: (1) gold deposition, (2) photoresist coating, (3) holographic-exposure, and (4) ion beam etching.

The basic steps for fabricating the surface grating are shown in Figure 38. The primary mirror blank is prepared with a reflective gold coating (0.5 μ m thick). A Hughes proprietary buffer layer is applied over the gold surface to attenuate reflected waves during exposure to optimize the grating definition. The photoresist layer (0.4-0.5 μ m thick) is applied using a dip-draining technique in which the exit flow from a deposition tank containing the primary mirror is controlled to achieve uniformity. Proper control of the exit flow rate is required to correct coating thickness variations caused by substrate curvature, contact angles, cross-sectional area, and the height change of the photoresist level. The photo-sensitive resist layer is exposed to the complex interference of the object and reference beams of the aberration corrected construction optics design. This design is necessary to reduce large amounts of aberration in the sampled beam

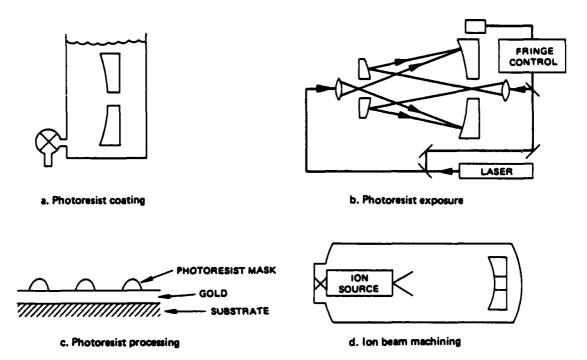


Figure 38. Basic surface grating fabrication steps.

caused by the difference between construction (0.4131 μ m) and use wavelengths (0.6328 μ m). The holographic exposure system, using a krypton ion laser, consists of construction optics and associated hardware assembled on a granite optical table isolated from mechanical and atmospheric vibrations. In addition, a real time fringe control system is used to ensure maximum interference contrast during the exposure. After processing, a relief photoresist grating is formed that exposes the gold surface. The final grating is transferred into the gold surface by ion beam etching through the photoresist mask. Excess photoresist is removed before subsequent usage.

3.2 DIP DRAINING PHOTORESIST DEPOSITION

3.2.1 Concept

Spin coating is the conventional method of photoresist deposition on small area flat substrates. The photoresist is deposited onto the substrate and spun at very high rpm (3000) spreading the photoresist uniformly over the surface. Because of the size and the angular velocity variation across the mirror surface, this method is not feasible with large substrates. The

dip draining photoresist deposition technique is a more complex coating process but is applicable to large area non-flat surfaces.

The dip draining photoresist deposition concept used for HOLAB is shown in Figure 39. The basic flow equation governing the system, neglecting frictional losses, is flow (Q) = velocity (V) x cross sectional area (A). The velocity within the deposition tank corresponds to the vertical coating rate. The cross sectional area is the area of the photoresist surface mimus the cross sectional area of the substrate. As the photoresist is drained out of the deposition tank, the resist level decreases thereby coating the substrate. The substrate coating rate is the velocity at which the resist level travels across the substrate surface. Rapid coating rates yield thicker photoresist layers and slow coating rates yield thinner photoresist layers.

Coating rate is a function of the photoresist viscosity, substrate curvature, and cross sectional area. In addition to the coating rate, photoresist thickness is also a function of the contact angle (coating angle) because of interaction of surface forces between the substrate and photoresist. To achieve uniformity, a proper substrate coating rate, based on theoretical and experimental datas, must be maintained. Stability is required to avoid perturbation of the resist fluid during the coating process. A high level of

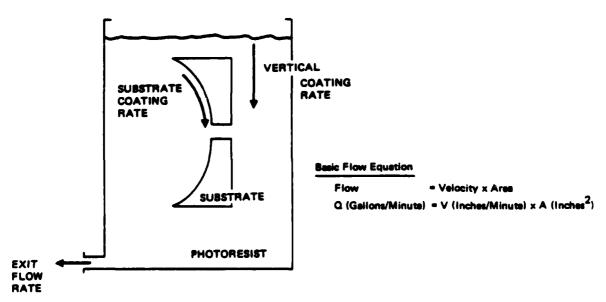


Figure 39. Dip draining parameters.

cleanliness is needed to minimize defects in the photoresist layer and proper venting prevents the resist vapor from attacking coated regions.

If the substrate is a flat optical surface with constant cross sectional area, a fixed exit flow would provide the proper substrate coating rate. A one-to-one relationship exists between the vertical and substrate coating rate. Compensation is required only for variation in the vertical coating rate because of potential energy loss as the resist level decreases. The cross sectional area and contact angle are fixed.

For circular, curved substrates, the substrate coating rate changes due to the curvature and cross sectional area of the substrate in addition to the potential energy loss. Since the substrate coating varies even with constant vertical coating rate, the exit flow rate must be altered during the coating process to achieve the proper substrate coating rate. Furthermore, the changing contact angle between the substrate tangent and the resist level affects the photoresist layer thickness. This effect required experiment investigation to determine the proper control required for a uniform photoresist layer.

3.2.2 System Design, Fabrication, and Test

The dip draining system is shown in Figures 40 and 41. The stainless steel deposition tank is 6 by 18 by 20 inches high. The exit flow of photoresist is monitored and corrected by a control subsystem, which consists of a venturi, pressure transducer, feedback control electronics, and an electro-pneumatic valve. The differential pressure at the venturi is compared to a reference differential pressure setting. Difference between the monitored and reference pressure causes the feedback control electronics to generate an error correcting signal to the electro-pneumatic valve. For stability, the deposition tank, venturi, and control valve are assembled on a vibration isolation table. During the coating process, the photoresist is emptied into a ballast tank. Before recycling the resist to the deposition tank, it is cleaned through a filtration subsystem. A cartridge filter with 1 µm pore size is used routinely. Increased cleanliness can be achieved if a high particle retention disk filter with 0.2 µm pore size is used. To aid in drying and to prevent vapor attack of coated regions, a venting

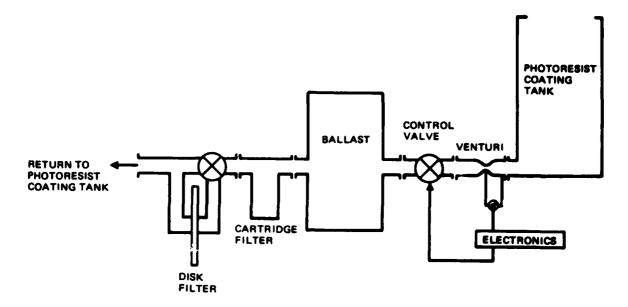
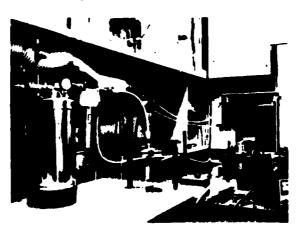


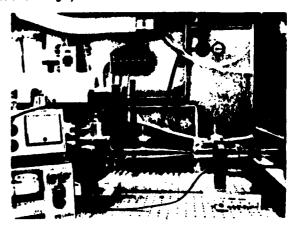
Figure 40. Dip draining photoresist deposition system schematic.



a) Dip draining photoresist coating system



b) Filtration subsystem



c) Control subsystem

Figure 41. HOLAB dip draining photoresist coating system hardware.

subsystem provides mild suction through two vertical vent tubes along the side walls of the photoresist deposition tank.

Because of the chemical makeup of photoresist and the need to use acetone for cleaning, high corrosion resistance materials were selected for fabricating the dip draining system. Stainless steel, glass, polyethylene, polypropolyene, teflon and ethylene propylene rubber gaskets were used to maintain a high integrity system.

The commercial photoresist utilized in the dip draining system is Shipley 1350B. This resist is a solvent base solution that consists of n-butyl acetate, cello-solve acetate, xylene, and proprietary solids. Its kinematic viscosity is 4.5 centistokes. Because viscosity can affect photoresist thickness, this characteristic is measured and corrected with photoresist thinner frequently.

The maximum flow rate and photoresist thickness that can be achieved are determined by the combination of the dimensions of the dip draining deposition tank, the exit port diameter, and the maximum opening of the electropneumatic valve. This maximum exit flow rate, Figure 42, is a function

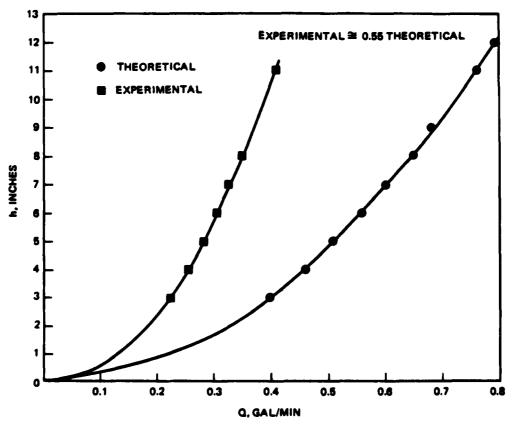


Figure 42. Photoresist exit flow rate variation in deposition tank.

of the potential energy or height of the photoresist level. The measured flow rates are 0.55 of theoretical calculated datas, which is attributed to frictional loss at the 1 inch diameter exit port of the deposition tank. The curve represents the maximum operating range of the dip draining system. If the lowest point of the substrate is situated 3 inches above the exit port, then the maximum vertical coating rate would be 0.43 inch/minute corresponding to 0.2 gallons/minute exit flow rate. For all other regions of the substrate, 0.43 inch/minute vertical coating rate would require less than maximum valve opening. This coating rate is expected to increase somewhat because of the cross sectional area of the substrate, but the exit flow rate will remain the same at each photoresist height level.

The venturi is fabricated from glass to a diameter ratio of 0.125 (1 to 0.125 inch). The flow through the venturi and the exit flow is dependent on the differential pressure. Experimental and theoretical curves of the pressure differential as a function of the exit flow rate are in close agreement as shown in Figure 43. The pressure transducer has a maximum reading of 1 psi with a sensitivity of 0.1 psi/volt. The electro-pneumatic valve is current controlled (15-50 mA) and actuated by pneumatic pressure. An electro-pneumatic valve was selected for its smooth actuation action to avoid subtle disturbances that can be transmitted back into the deposition tank.

The dip draining system was set for constant exit flow with a reference differential pressure of 0.2 psi that corresponds to a 0.25 inch/minute vertical coating rate. The monitored differential pressure during the test run is shown in Figure 44. The control subsystem could compensate for the reduced photoresist level height by increasing the valve opening over 17 inches of coating area.

In another test, preliminary photoresist coating thickness was measured for a reference pressure differential of 0.3 psi corresponding to a vertical coating rate of 0.44 inch/minute. Photoresist thickness measured on flat $(2 \times 3 \text{ inches})$ samples were approximately 4400 Å. This photoresist thickness was sufficient to achieve the shallow ion beam etching depths required for the beam sampling grating.

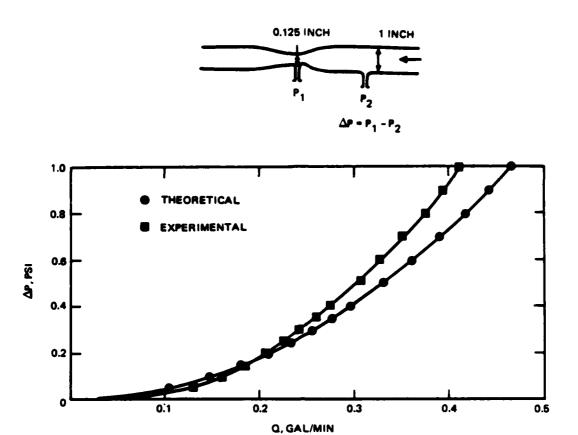


Figure 43. Exit flow rate effects on venturi differential pressure indications.

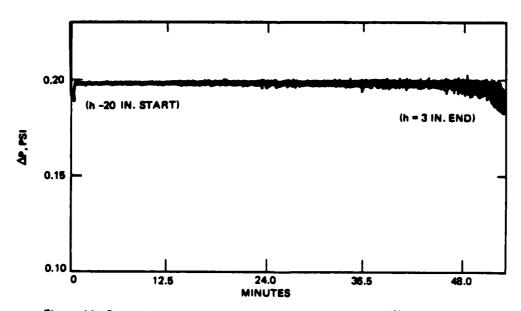


Figure 44. Control subsystem capability to maintain constant differential pressure.

3.2.3 Analysis of Photoresist Deposition on a 30 cm Diameter f/1.5 Parabolic Mirror

In a dip draining photoresist deposition system, the substrate is oriented vertically within the photoresist deposition tank. As resist is allowed to drain out, the level of the photoresist decreases thereby coating the substrate. Thickness is a function of the substrate coating rate and angle. With a fixed exit flow, this coating rate varies because of the substrate curvature and cross sectional area. The variation can be computed theoretically and the exit flow regulated to achieve a constant coating rate. The coating angle of the substrate also varies due to surface curvature. Its effect on photoresist thickness must be assessed experimentally to optimize uniformity with a variable coating rate across the substrate surface.

The equation describing the surface of a 30 cm diameter parabolic mirror with a focal length of 17.72 inches is $x^2 + y^2 = 70.88$ z where the parabolic surface lies in the x-y plane with its center at the origin and the optical axis along the z axis. Contact angle versus the substrate vertical position along the y axis is shown in Figure 45. The contact angle is between the substrate surface tangent and the normal to the photoresist level. The contact angle increases from 0 degrees at the center toward ± 10 degrees at the extremes of the substrate. Along a horizontal plane across the substrate, the contact angle is constant, i.e., $\theta = \text{constant}$ for all values of x.

Substrate curvature affects both coating rate and coating angle. The substrate coating rate will always be higher or equal to the vertical coating rate, the rate of change in the level of the photoresist within the deposition tank. The ratio of the substrate coating rate to the vertical coating rate (ds/dy) is plotted in Figure 46. At the center of the substrate, where the surface tangent is vertical (0 degree contact angle), a one-to-one correspondence exists between the vertical and substrate coating rate. With a constant exit flow, the coating rate with respect to the center increases toward the top and bottom of the substrate by 1.014X.

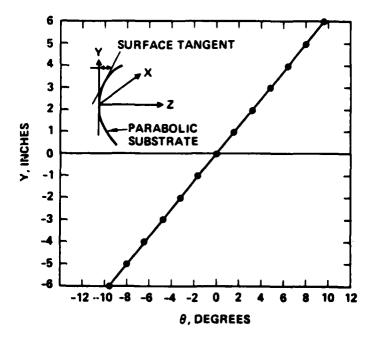


Figure 45. Contact Angle Variation for the HOLAB Mirror.

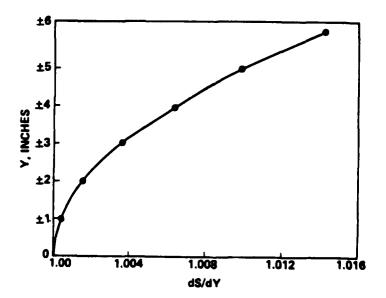


Figure 46. Variation in Substrate Coating Rate for Fixed Vertical Rate.

Photoresist thickness is also affected by the variation in coating angle act angle due to the substrate curvature. Different surface force disnutes the photoresist and the substrate is created for various angles as evident by the change in the miniscus shape at the interface ubstrate and photoresist. Photoresist thickness was obtained experiyas a function of contact angles and substrate coating rate. These re used to determine the variable substrate coating rate profile d to optimize photoresist thickness uniformity.

The horizontal cross sectional area of the parabolic substrate varies action of vertical height contributing to coating rate errors. From the ow equation, with a constant exit flow, the vertical coating rate changes by to the cross sectional area of the photoresist surface area. The sist surface area is maximum toward the top and bottom edge of the te and minimum at the center where the substrate cross sectional area est. The change in substrate coating rate caused by the cross secreta of the substrate, normalized to the central rate for a 2 inch thick ic substrate, is shown in Figure 47. With a constant exit flow, the

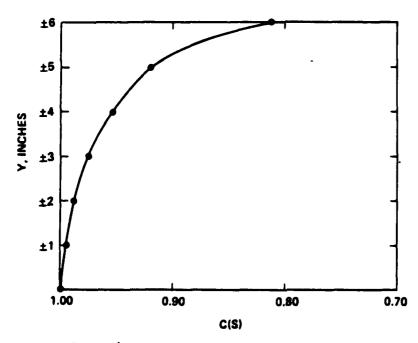


Figure 47. Variation in Substrate Cross Sectional Area.

coating rate with respect to the center decreases toward the top and bottom of the substrate by 0.812X.

The combined effect of substrate curvature and cross sectional area on coating rate is given in Table 12. Coating rate increases toward the top and bottom of the substrate with respect to the center due to curvature. Coating rate decreases toward the top and bottom with respect to the center due to the substrate cross sectional area. More variation is attributed to cross sectional area changes. Some balance exists when the combined effects are multiplied. To achieve a uniform substrate coating rate, the exit flow should start off 0.824X the central rate and gradually increase as the coating progresses toward the center and decreasing again toward the bottom.

The approach taken for coating the HOLAB primary mirror was to use the control electronics to maintain a constant exit flow. The control system then is greatly simplified since only one ΔP has to be maintained for all h. The substrate was coated with a flow rate of 14 in minute corresponding to a ΔP of 0.045 psi. At the horizontal plane containing the vertex of the primary mirror, the vertical coating rate is 0.177 inch/minute decreasing to 0.141 inch/minute at the extremes of the primary mirror because of increasing photoresist cross sectional area. The photoresist thickness profile as a function of h, from coating rate analysis, is shown in Figure 48.

TABLE 12. VARIATION IN SUBSTRATE COATING RATE WITH CONSTANT EXIT FLOW

Substrate	Cross Sectional Area, C(S)	Curvature, d(S)/d(Y)	$C(S) \times d(S)/d(Y,$
±6 inch	0.812	1.0142	0.824
± 5	0.921	1.0099	0.930
±4	0.954	1.0063	0.960
±3	0.975	1.0036	0.979
±2	0.990	1.0016	0.992
±1	0.994	1.0004	0.994
0	1.000	1.0000	1.000

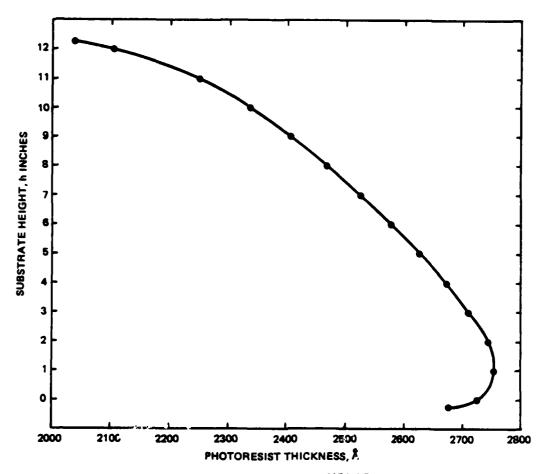


Figure 48. Photoresist thickness profile on HCLAB primary mirror with constant differential pressure (ΔP) control.

The photoresist thickness is 2579°A at the center of the substrate, decreasing over the top half of 2109°A, and increasing over the bottom half of the substrate to 2753°A.

3.3 HOLOGRAPHIC EXPOSURE

3.3.1 Holographic Grating Construction Optics Design

The holographic grating construction optics for HOLAB are presented in Figure 49. Points A and B are conjugate coherent laser beam point sources necessary to form the interference pattern on the primary mirror. The distances of these points from the mirror combine to define the hologram focal length. Out of the infinite sets of conjugate distance pairs that give the desired focal length, there is one pair of conjugate distances such that holographic grating formed provides minimal spherical aberration in the

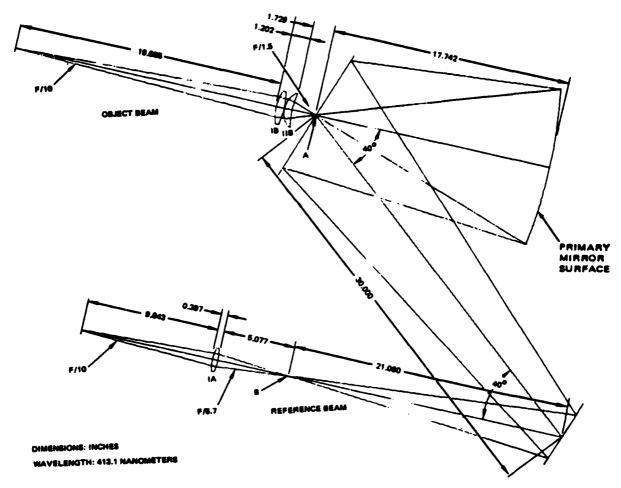


Figure 49. Holographic grating construction optics configuration.

playback sample beam; this pair is selected as the design starting point. Spatial filter burn out and position sensitivity restrict the available laser beam divergence to about F/10, whereas the required reference beam and object beam divergence are F/5.7 and F/1.5, respectively. Thus beam diverging lenses are used in both beams. The curvatures of these lenses together with the conjugate point sources are optimized for minimum spherical aberration of the sample beam. Construction optics sensitivities are given in Tables 13 and 14.

As shown in Figure 49, the object beam goes through a positive twoelement beam diverger to produce the F/1.5 beam to illuminate the primary mirror; the reference beam source is at a longer distance from the primary mirror and passes through a single element beam expander to expand the

TABLE 13. CONSTRUCTION OPTICS MANUFACTURING SENSITIVITIES

		Change	Sample Bea Aberration (
Parameter	Nominal Value		Comatic(\lambda)	Spherical(λ)	Focal Adjustment
Reference Beam	2. 956 in.	±0.003 in.		0.02	0.000 in.
Lens IA Radius	4.690 in.	±0.005 in.		0.01	0.000 in.
Object Beam	3.712 in.	±0.004 in.		0.01	0.000 in.
Lens IB Radius	5.517 in.	±0.006 in.		0.02	0.000 in.
Object Beam	1.605 in.	±0.002 in.		0.01	0.002 in.
Lens IIB Radius	5.370 in.	±0.005 in.		0.01	0.000 in.
Reference Beam Lens IA Thickness	0.397 in.	±0.002 in.		0.00	0.000 in.
Object Beam Lens IB Thickness	0.591 in.	±0.002 in.	}	0.00	0.000 in.
Object Beam Lens UB Thickness	0.592 in.	±0.002 in.		0.00	0.004 in.
Reference Beam Lens IA Wedge	0	±0.6 mrad	0.08		0.
Object Beam Lens IB Wedge	o	±0.6 mrad	0.31		0.
Object Beam Lens IIB Wedge	0	±0.6 mrad	0.64		0.
Reference Beam Lens IA Index	1.519	±0.001		0.03	0.001 in.
Object Beam Lens IB Index	1.519	±0. 001		0.15	0.003 in.
Object Beam Lens IIB Index	1.519	±0.001		0.27	0.007 in.

^{*}Focus adjustment is performed by moving the collimating lens group axially along the optical axis

TABLE 14. CONSTRUCTION OPTICS ALIGNMENT SENSITIVITIES

			Sample Beam Wavefront Aberration ($\lambda = 0.6328 \mu m$)		_
Parameter	Nominal Value	Change	$Comatic(\lambda)$	Spherical(\lambda)	Focus Adjustment*
Reference Beam Distance: Point Source to Lens IA	19.685 in.	0.010 in.		0.02	0.000 in.
Reference Beam Distance: Lens IA to Primary Mirror		0.010 in.		0.11	0.001 in.
Object Beam Distance: Point Source to Lens IB	9.843 in.	0.010 in.		0.00	0.000 in.
Object Beam Distance: Lens IB to Lens IIB	0.020	0.001 in.		0.02	0.001 in.
Object Beam Distance: Lens IIB to Primary Mirror		0.010 in.		0.31	0.013 in.
Reference Beam Lens IA Tilt	0°	0.5 mrad	0.01		0
Object Beam Lens IB Tilt	00	0.5 mrad	0.18		o
Object Beam Lens IIB Tilt	o°	0.5 mrad	0.31		o
Reference Beam Lens IA Decenter	0	0.001 in.	0.06		0
Object Beam Lens IB Decenter	0	0.001 in.	0.16		o
Object Beam Lens IIB Decenter	0	0.001 in.	0.57		o
Reference Beam Decenter Relative to Primary Mirror	o	0.010 in.	0.10		0
Object Beam Decenter Relative to Primary Mirror	o	0.010 in.	6. 33		0
Primary Mirror Tilt	0	0.1 mrad	0. 26		0

^{*}Focus adjustment is performed by moving the collimating lens group axially along the optical axis

laser beam from F/10 to F/5.7. The linear dimensions from the laser beam sources to the vertex of the primary mirror are 40.358 inches for the object beam and 84.119 inches for the reference beam. For a compact optical bench setup, the reference beam is folded by two plane-mirrors so that thereference beam is parallel to the object beam with a separation of 19.284 inches. The folding mirror near the beam expander of the object beam has a nole to let the object beam pass through. This configuration minimizes obscuration difficulties. Furthermore, stops located at the intermediate foci of the two beams can be used to minimize stray light (both diffracted and scattered) that can cause spurious holograms to be recorded. Because the object beam and the reference beam are colinear with the optical axis of the primary mirror, the design task is much simplified. The glasses of the beam expander lenses were selected to be Schott BK7 because of its high transmittance at the construction wavelength 413 nm, and no aspheric glass surfaces were required.

3.3.2 Exposure Configuration

The HOLAB holographic grating recording system, aligned onto a granite optical table, 72 by 144 by 18 inches thick, is shown in Figure 50. The table, supported with low resonance frequency pneumatic mounts, is decoupled from floor and building vibrations. Atmospheric disturbances are attenuated with an acoustic shield enclosure around the perimeter of the table. In addition, horizontal laminar flow within the room ensures environmental cleanliness.

The substrate and the interfering wavefronts used to record a holographic beam sampling grating must remain stable to fractional wavelength dimensions to optimize recording contrast. Similarly, in conventional photography, the film and subject must remain still when the shutter is open to avoid blurring. Interference instability can be caused by phase errors due to construction optics and mount motions. A quarter wave motion on any reflective optics would introduce a 180 degree phase error between the construction wavefronts, causing corresponding maximum and minimum interference locations to interchange. The result of this motion is reduced



Figure 50. HOLAB holographic grating exposure system.

contrast, non-uniformity and under-exposure. For the HOLAB recording, the grating dimension at the edge of the substrate is approximately 1.5 μ m/cycle. Thus the substrate must have in-plane stability to a fraction of this feature size.

To ensure maximum recording grating contrast, the stability of optical mounts within the recording system is interrogated and confirmed by interferometric testing of each mount for positional stability. Residual phase shift, caused by acoustical perturbations and slow mirror and mount expansions, is compensated via an electronic feedback fringe control system that detects and corrects phase errors in real time during exposure. The electronic controller works in conjunction with an interferometer that monitors the relative phase difference between a small segment of the

construction wavefronts near the exposure plane. Errors are corrected by modulating a piezoelectrical translator within one of the construction beams to stabilize the recording fringes at the exposure plane.

The 0.4131 µm wavelength output from a Spectra-Physics Model 171-01 Krypton Ion laser is used to expose the photoresist. At the recording 0.4131 µm wavelength, the optimized TEM₀₀ mode output is 1.45 watts. The temperature stabilized etalon reduces this output to 1 watt at single frequency operation where coherence length is >1 km.

Meticulous alignment of construction optics is required to avoid introducing additional aberration in the sampled beam upon playback at the 0.6328 µm wavelength. Conventional tools, theodolite, and gauge rods, were used to align the construction optics to set their separation, lateral displacement, and tilt to the tolerance established by the grating design. An alignment fixture, installed in the central hole and aligned to the optical axis of the primary mirror, aided in aligning the substrate with respect to the construction optics. The optical axis of the recording system was 10 inches above the table surface.

Before exposure, the two paths of the construction optics are adjusted radiometrically so that each path provides equal irradiance at the primary mirror. Adjustments to the optical elements before the spatial filters are used to provide adequate irradiance uniformity over the primary mirror aperture. Construction optics are carefully cleaned. A high degree of cleanliness is required on the construction optics, lenses, and mirrors to minimize spurious groove structures due to diffraction from contaminants.

Test exposures were performed with 2 by 3 inch flat substrates. These substrates were deposited with gold and a proprietary buffer coating to eliminate standing waves for improved grating definition. The substrates were then coated in the dip drain photoresist deposition system with a 2200Å layer of 1350B photoresist. The photoresist was then baked at 60°C for two hours to remove excess solvents. The photoresist was exposed to the holographic interference in the recording system. After exposure, the samples were processed in AZ developer for 2 minutes. The developer removes photoresist in high exposure regions; a relief photoresist grating structure is left on the metal surface for subsequent ion beam etch transfer

of the grooves to the gold surface. After development, the samples were rinsed for 10 minutes in de-ionized H₂O and nitrogen dried.

Results of the test substrate exposures from SEM interrogation are given below:

2.63 mj/cm ²	severely underexposed
4.29 mj/cm ²	considerably underexposed
5.90 mj/cm ²	moderately underexposed
8.00 mj/cm ²	0.62 duty cycle
10.00 mj/cm ²	0.50 duty cycle
13.35 mj/cm ²	0.41 duty cycle

The test exposures provided the exposure energy calibration required for complete removal of photoresist at the bottom of the grating structure with a duty cycle of approximately 0.4 as specified by the efficiency design for a nominal 10 percent diffraction efficiency. In addition, the test exposures confirmed adequate stability of the recording system for producing submicron dimension groove spacing and verify proper beam ratios, beam uniformity, and laser stability.

3.4 ION BEAM ETCHING

The holographically exposed photoresist grating on the evaporated gold surface of the HOLAB parabolic primary mirror is a mask for ion beam etching that transfers the grating into the metal surface. This process produces the ultimate depth and delineation of the grating on the mirror surface.

An in-house dc ion beam source, 0.5 cm, Veeco Microetch, Figure 51, was used. Since the uniform beam yielded by this source is only 2 inches in diameter at about 4 inches from the grid exit of the source, the substrate must be moved approximately 12 inches further away. At this distance the less intense, divergent beam expands the uniform beam density pattern to approximately 4 inches in diameter and falls off only slightly at about 6 inches diameter. With the same power and pressure settings on the source, this beam pattern is better than 90 percent repeatable.

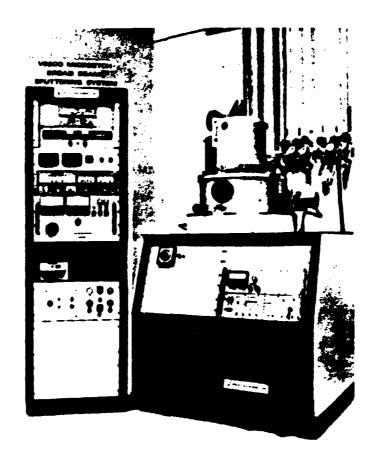


Figure 51. Ion beam etching system used for HOLAB.

The mirror to be etched was placed on a rotary table at this precalibrated distance from the source and rotated uniformly underneath at stationary, shaped aperture. The aperture is preshaped, and only a radial section of the mirror is opened to the beam. This opening is wedge shaped; the inside width to the outside width of the aperture is a very rough proportion of the inner hole circumference to the outer circumference of the mirror. Several calibration runs were made with samples, and the aperture is reshaped between each test run until a uniform depth is obtained across the aperture required for the mirror. These trial runs also provided an accurate etching rate for the gold surface.

During the ion beam etching of the HOLAB mirror, monitors were placed at the circumference of the inner hole and at the outside circumference of the primary mirror. These monitors provided a measure of the etching rate as well as confirming the final grating depth. After an etch depth of 532Å was measured on monitor samples, the photoresist pattern was chemically stripped off the mirror. The substrate was then reinserted into the Microetch system and the 100Å of proprietary buffer layer, used for standing wave reduction during the holographic exposure, was etched off.

3.5 THE HOLAB GRATING FABRICATION EXPERIENCE

After optimization and calibration of the various fabrication steps, the beam sampling grating fabrication effort for the HOLAB, 30 cm diameter, F/1.5 parabolic primary mirror was initiated. Optical coatings on the substrate were deposited via EB evaporation. The coatings consisted of $0.5\,\mu\mathrm{m}$ of gold overcoated with an antireflection buffer layer for standing wave reduction to improve grating definition. The nominal photoresist coating thickness, applied by dip-draining, was $2431\text{\AA} \pm 322\text{\AA}$. After coating, the photoresist was baked at $60^{\circ}\mathrm{C}$ for 2 hours. The Krypton ion laser with 0.6 watt output at $0.4131\,\mu\mathrm{m}$ wavelength was used for holographically exposing the grating in the photoresist film. Irradiance uniformity was 10 percent with a beam ratio of 1.26 (recording contrast greater than 99 percent). Exposure time for $14\,\mathrm{mJ/cm}^2$ energy density was 35 minutes and 34 seconds. Following exposure, the photoresist was developed in AZ developer for 2 minutes at $20^{\circ}\mathrm{C}$, rinsed in deionized water and dried. The ion beam etching depth was calibrated at $530\text{\AA} \pm 10$ percent.

Before the HOLAB grating was fabricated, a 30 cm diameter, F/2.0 spherical mirror was coated and exposed with 10 mJ/cm². After subsequent development, the grating seemed to be underexposed. It was decided to continue the HOLAB grating fabrication, however, the exposure energy was adjusted. In retrospect, the failure of this attempt probably was caused by the differing reflectivity from the substrate surface (compared to subscale calibration samples) that could have been caused by differences in the antireflection buffer coating or the commercial gold coating.

Increased reflectivity would cause standing waves formation parallel to the substrate. Subsequent development was retarded because of the stepwise removal of photoresist through high and low standing wave nodal exposure energy planes.

The first grating fabrication attempt with the HOLAB primary mirror was exposed with an increased 15 mJ/cm² energy. During development, the resist grating completely washed off in the developer in a very short time. Then the substrate was cleaned chemically and within an oxygen plasma. A second attempt, using a lower 10 mJ/cm² of exposure energy, exhibited similar problems.

Radiometric recalibration of the exposure energy was done by exposing the primary mirror substrate in four segments with 4, 8, 12, and 16 mJ/cm² of exposure energy. After development under microscopic inspection, the cause of the photoresist grating wash off was attributed to adhesion failure due to surface contamination of the upper optical coating. In underexposed regions, where the resist grating did not break through to the substrate optical coating, the photoresist remained intact. When the resist grating broke through to the substrate optical coating with increased exposure, the photoresist washed off during development because of reduced contact area between the photoresist and the substrate. The duty cycle determined from small remaining areas of gratings on the substrate within the four segments confirmed previously calibration data from subscale samples.

In an attempt to remove the unidentified surface contaminant, an in-house RF sputter system was used to etch a small amount of material from the top optical coating. Using an exposure energy of 14 mJ/cm², considerable improvement over previous results was noted. The wash off of the photoresist grating occurred after a longer period within the developer, and an increased area of grating adhered to the substrate. A second attempt using this cleaning method improved grating adhesion such that only a small segment of the 30 cm diameter grating aperture exhibited failure.

Because the cleaning processes were not uniform, the optical coatings were noticeably affected. The inner radial region was completely stripped of the buffer coating by the oxygen plasma system thereby exposing the gold. Since etching within the RF sputter system was preferential toward the outer radial region, the antireflection buffer layer was completely removed and fresh coatings were evaporated again over the gold. The buffer was removed by ion beam etching within the Veeco-Microetch system, which was calibrated for uniform etching of the grating into the gold surface of the substrate.

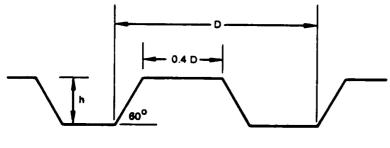
An antireflection buffer coating was reevaporated onto the gold. Then with fabrication conditions that were similar to that used in previous trials, and determined by subscale calibration samples, this attempt was successful. The photoresist was exposed with 14 mJ/cm 2 of energy. Under microscopic inspection, the duty cycle was approximately 0.45 to 0.55. Grating periods ranged from approximately 1.5 to 10 μ m per cycle. In addition, the effectiveness of the antireflection buffer layer produced very high grating edge acuity.

The grating was then ion beam etched into the gold surface to a depth of 530\AA for a nominal 10 percent diffraction efficiency at the 0.6328 μm wavelength of the probe (HeNe) beam. The excess photoresist was removed chemically, and the substrate was exposed to the ion beam. Then the residue buffer coating previously masked by the photoresist grating was removed. The primary mirror was then installed within a mounting fixture for the HOLAB breadboard.

3.6 HOLOGRAPHIC GRATING PERFORMANCE

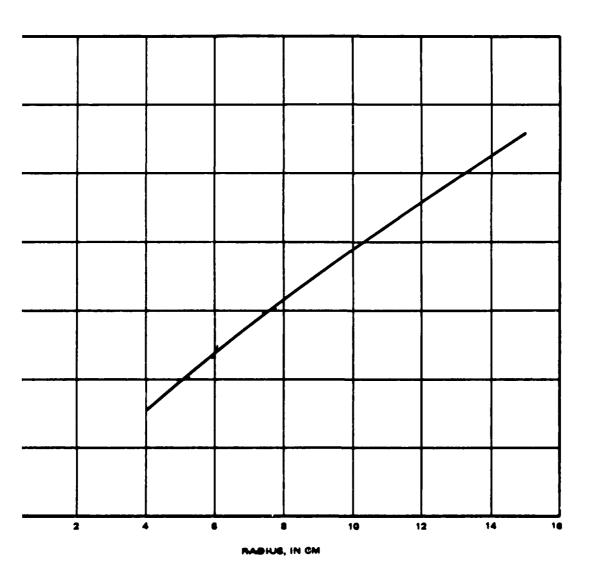
3.6.1 Diffraction Analysis

The diffraction efficiency of the primary mirror holographic grating has been calculated, as a function of radial position for s and p polarized light, for $\lambda = 0.6328\,\mu$. The groove model assumes the geometry shown in Figure 52. The inputs to the calculation included the grating frequency (related to the linewidth, D) and incident and diffracted angles as a function of radial position. A plot of the grating frequency versus radius is presented in Figure 53. The diffraction efficiency of the sample beam (-1 order) and



h = 0.084 λ (CHOSEN TO GIVEN APPROXIMATELY 10% DIFFRACTION EFFICIENCY)

Figure 52. Diffraction grating groove model.



Marian BE. Makasarahka asatina financasay wasus radius.

the outgoing beam (zero order) as a function of radial position for s and p polarisations is presented in Table 15. The diffraction efficiencies of both polarisations are seen to be quite uniform over the entire aperture. The diffraction efficiency of the outgoing beam (zero order) for incident light with $\lambda=2.7~\mu{\rm m}$ is presented in Table 16. The outgoing beam at $\lambda=2.7~\mu{\rm m}$ loses 2 to 5 percent and 1 to 3 percent of the incident energy contained in s and p polarisations, respectively. The diffracted angle and diffraction efficiency as a function of diffraction order at a radius of 10 cm is presented in Table 17. The table shows that the +1 order also has a high diffraction efficiency but that the direction of this order is far removed from the -1 order.

TABLE 15. THEORETICAL DIFFRACTION EFFICIENCIES AS A FUNCTION OF APERTURE LOCATION ($\lambda = 0.6328 \mu m$)

	Diffraction Efficiency (in percent)				
Aperture	-1 o	rder	0 order		
Radius (cm)	TE	TM	TE	TM	
4	9.5851	9.4563	76.835	75.694	
5	9.6178	9.4109	77.201	75.750	
6	9.6442	9.7105	77.558	75, 111	
7	9.6558	9.6069	77.919	75.081	
8	9.7088	9.6284	78.275	75.941	
9	9.7362	9.9069	78.668	74, 205	
10	9.7019	10, 141	78.971	75.793	
11	9.6933	10, 245	79.321	74.579	
12	9.7393	10.671	79.842	71.558	
13	9.8129	9. 5029	80.132	77.052	
14	9.8271	9. 8529	80.394	76.617	
15	9.8272	10.048	80.681	75. 985	

TABLE 16. DIFFRACTION EFFICIENCY OF THE OUTGOING BEAM (ZERO ORDER) AS A FUNCTION OF RADIAL POSITION (λ = 2.7 μ m)

Radius	Diffraction Efficiency (Zero Order) in Percent		
in cm		P	
15	97. 33	99.01	
14	97.87	98.93	
13	94.44	98.36	
12	95.55	98.07	
11	96.06	97.86	
10	96. 38	97.70	
9	96.64	97.57	
8	96. 45	97.44	
7	96. 38	97.33	
6	96.62	97.22	
5	96. 22	97.06	

3.6.2 Diffraction Uniformity Measurement

Introduction. In an effort to characterize the HOLAB holographic grating, the relative efficiency of the HOLAB grating was measured over most of its aperture. Any large variation in efficiency could exercise the automatic gain control on each aperture of a typical Hartmann-type wavefront sensor. Potentially pointing errors caused by any small nonlinearities present in the system could be produced.

Method. Efficiency measurements were made by masking off all but a 0.25 inch diameter portion of the HOLAB input beam. This size was chosen to closely simulate the relative portion of the aperture that would be seen by an individual sub-aperture of a typical wavefront sensor. The test geometry is shown in Figure 54. An aluminum plate with a 0.25 inch diameter perforation was mounted in the path of the input laser beam at "M" in the figure. The energy transmitted by the aperture was measured at locations

TABLE 17. DIFFRACTION ANGLE AND EFFICIENCY AS A FUNCTION OF DIFFRACTION ORDER ($\lambda = 0.6328 \mu m$, RADIUS = 10 cm)

	*Diffraction Angle in Degrees	Diffraction Efficiency (in percent)		
Order		•	р	
-4	-53,53	1.56	0.23	
-3	-35, 13	0.68	0.64	
-2	-20.30	1.23	0.45	
-1	- 6.79	10. 15	9.72	
0	6.34	76. 15	78.81	
1	19.82	8.76	9.27	
2	34.59	1.05	0.38	
3	52.78	0.46	0.51	

*Sign Convention

 $\sin \phi_{\mathbf{d}} = \sin \phi_{\mathbf{i} \mathbf{n}} + \frac{n\lambda}{D}$

φ_a = diffracted angle

 ϕ_{in} = incident angle

 λ = wavelength

D = line width

n = integer

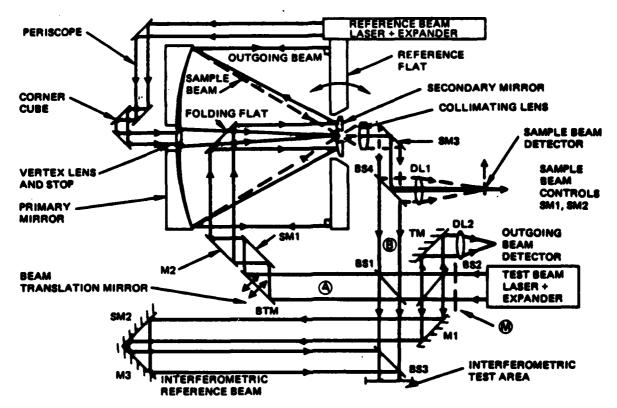


Figure 54. HOLAB measurement schematic.

"A" and "B" by a UDT power meter and the values were recorded. Then the aperture was moved to various positions in the beam by an x-y translation stage, and the procedure was repeated.

Results. As indicated in Figure 55, valid data points were recorded over the surface of the grating. The location of each data point and the power values recorded appear in Table 18, along with the calculated efficiency, and the scaled efficiency, ke, reflecting the additional losses incurred in the beamsplitters and optical components other than the grating.

The grating was very uniform, with the absolute efficiency of all measurements lying between 7 and 8 percent. The average efficiency was 7.4 percent with an RMS deviation for each point of 0.2 percent. The final three data points appear to differ significantly from the average value and may represent a "hot spot" on the grating. If these points are eliminated from the computation, an average efficiency of 7.33 percent with an RMS deviation of 0.13 percent is computed from the remaining data, indicating a very uniform grating over most of the aperture.

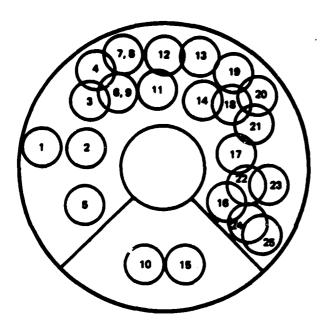


Figure 55. Subsperture measurement locations on the HOLAS grating.

TABLE 18. EFFICIENCY DATA

	x(mm)	y(mm)	P _{in} (μW)	P _{out} (µW)	€ (%)	k∈(%)
1	17. 47	0.8	40.6	0.71	1.76	7. 13
2	11.60	0.8	66. 8	1.23	1.84	7.45
3	11.60	7. 1	55. 4	1.02	1.84	7.45
4	11. 60	11.0	40.7	0.73	1.79	7. 25
5	11.60	-5. 6	64.9	1. 19	1.83	7.41
6	8. 25	7. 1	63. 3	1. 13	1.79	7. 25
7	8. 25	13.0	40.7	0.73	1.80	7. 29
8	8. 25	13.0	42.8	0.79	1.85	7.49
9	8. 25	7. 1	65. 8	1. 18	1.79	7. 25
10	2. 25	-11.9	68. 7	1.25	1.82	7.37
11	2. 25	8.4	49.8	0.88	1.77	7. 17
12	2. 25	13. 5	36.4	0.66	1.82	7. 37
13	-3.75	13. 5	23.4	0.41	1.75	7.09
14	-3.75	7. 1	37. 7	0.67	1.77	7. 19
15	-3. 75	-11.9	50.0	0.93	1.86	7. 55
16	-9.75	-5. 6	33. 5	0.62	1.85	7.48
17	-9.75	0.8	30. 5	0.56	1.80	7. 29
18	-9.75	7. 1	22. 1	0.40	1.80	7. 28
19	-9. 75	11.0	16. 9	0.31	1.82	7. 37
20	-11.87	10.2	14.4	0.26	1.82	7. 36
21	-11.87	6. 3	18. 1	0. 32	1.78	7. 19
22	-11.87	0.0	22. 1	0.41	1.87	7.5~
23	-14.9	0.0	9.8	0. 19	1.93	7.81
24	-11.87	-6.4	19.9	0. 39	1.96	7. 93
25	-13.6	-7.6	11.9	0. 23	1.93	7. 82

The measurement error is estimated to be 0.1 percent in relative efficiency, based on the repeatability of the power measurements made. The error in absolute efficiency may be as high as 20 percent relative to the measured efficiency, due to the estimate of the required optical transmission. This error is identical for each measurement and reflects only on the uncertainty on the scaling factor "k" used to relate measured efficiency to absolute efficiency of the grating.

The data points are plotted in Figure 56, grouped into sets of points with similar y-positions. The grating efficiency over the entire aperture is plotted in Figure 57, illustrating the "hot spot" in the lower left-hand corner of the grating, as well as the general center to edge uniformity variation.

Conclusions. The HOLAB grating was very uniform in diffraction efficiency over its clear aperture. The measured RMS nonuniformity is well within the linear range of a typical wavefront sensor AGC. Only one area on the grating departed significantly from the average efficiency, and this departure of 0.5 percent absolute (7 percent relative) is small compared to the error budgeted for nonuniformity in fabrication. The remaining variations indicate a general trend of lower efficiency near the center; however, no statistically significant correlation could be found.

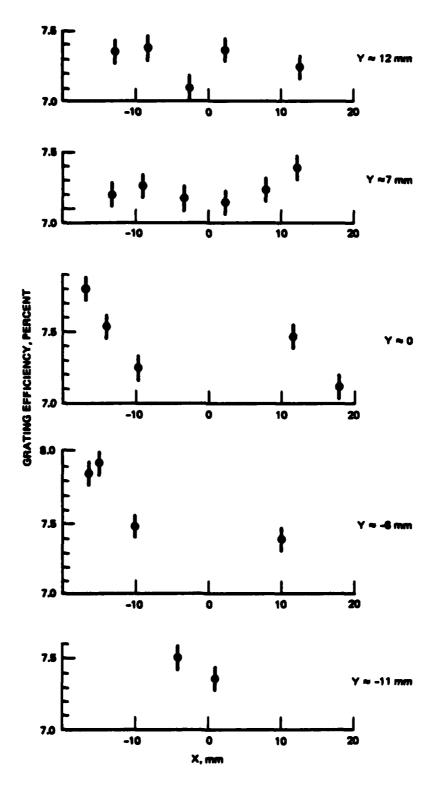


Figure 56. Grating efficiency measurements.

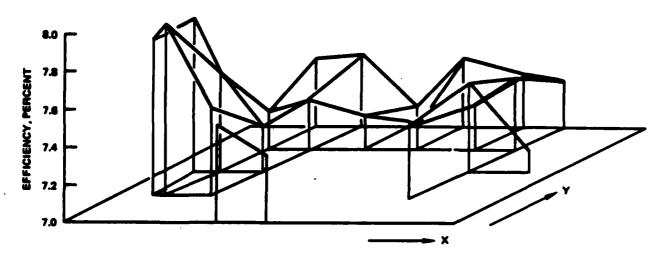


Figure 57. HOLAB grating efficiency.

SECTION IV EXPERIMENTAL RESULTS

4.1 EXPERIMENTAL PROCEDURES

Following preliminary alignment and checkout procedures, the HOLAB Breadboard was exercised to determine the operational performance of the holographic beam-sampling technique with the following perturbations:

- 1. One-axis manual off-axis steering of the beam expander
- 2. Manual defocus of the secondary mirror
- 3. Manual decenter of the secondary mirror, and
- 4. Deformation of the primary mirror substrate.

One-axis, manual, off-axis steering of the output beam from the HOLAB beam expander is accomplished by one-axis rotation of the reference beam laser, which is mounted to the reference flat and moves in unison with it. Rotations of the reference flat assembly maintain the alignment of the reference beam with respect to the reference flat, but cause rotations of the reference beam with respect to the optical axis of the beam expander. Secondary mirror defocus is accomplished by translation of the secondary mirror parallel to the optical axis of the primary mirror. Secondary mirror decenter is accomplished by translation of the secondary mirror perpendiculat to the optical axis of the primary mirror. Deformations are induced in the primary mirror optical surface by mechanical force loads applied to the back surface of the primary mirror.

During breadboard testing, perturbations may change the pointing direction of the sample beam relative to the pointing direction of the reference beam. Closed-loop operation of the test breadboard will cause steering mirrors SM1, SM2, and SM3 to drive the centroids of the focused sample beam and reference beam to be coincident and centered on the sample beam detector.

Any change in direction of the outgoing beam relative to the unperturbed condition is measured by use of a photopot detector placed in the focal plane of detector lens DL2 as shown in Figure 58. The measurement is made from the outgoing beam, which is retroreflected from the reference flat, travels on a return path through the beam expander, steering mirrors and beam translation mirror, and is then partially reflected at beamsplitter BS2.

Interferograms are taken to measure the effect of system perturbations on outgoing beam and sample beam wavefront quality. Outgoing beam interferometric measurements are made by photographically recording the interference of the retroreflected output beam and an interferometric reference beam. The interferometric reference beam is derived from the test beam laser through use of beamsplitter BS2. To obtain high contrast interference fringes at the interferometric test area, the intensities of the two beams were made to be approximately equal through a suitable choice of the

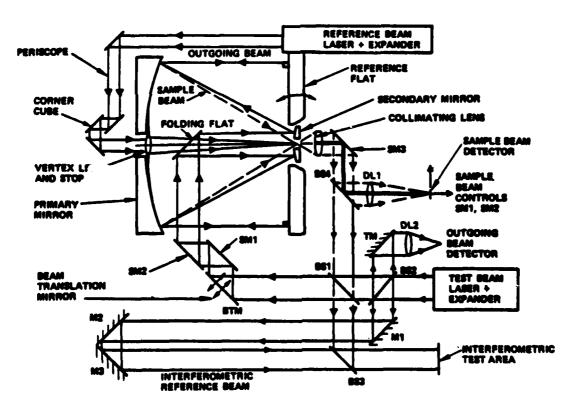


Figure 58. HOLAB optical schematic.

beamsplitting ratios for BS1, BS2, and BS3. In addition, the path lengths of the two beams were made approximately equal to ensure a high degree of coherence between the two beams, enabling high contrast fringes to be formed.

Sample beam interferometric measurements are similarly made by photographically recording the interference of the sample beam and the interferometric reference for the sample beam, with the outgoing beam blocked or beamsplitter BSI removed from the breadboard. Comparisons of the sample and outgoing beam wavefronts are made by computerized data analysis of the interferogram.

Thus, the experimental breadboard measures the ability of the holographic grating beam sampling technique to determine the outgoing beam direction and wavefront quality for a large aperture beam expander for a variety of different system perturbations and for a range of perturbation magnitudes.

4.2 WAVEFRONT QUALITY MEASUREMENTS

Interferograms were taken to determine effects on wavefront quality of the outgoing and sample beams for a variety of different system perturbations and for a range of perturbation magnitudes. The interferograms were taken with a camera located at the interferometric test area as indicated in the HOLAB optical schematic in Figure 58. Additional optical components used for taking output beam interferograms only are shown in Figure 59. Adding the lens and folding mirror just before the interferometric test area provides two advantages. First, the primary mirror aperture is reimaged by the lens on the film plane; thereby providing interferograms with better definition near the edge of the aperture. Secondly, the mirror corrects a reversion which would otherwise exist between the output beam and sample beam data. The output beam and sample beam interferograms included in this report correspond directly (i.e., the left side of the aperture is on the left side of the photo in both the output beam and sample beam interferograms) when the photos are oriented such that the strut shadows are in the lower portion of the photo.

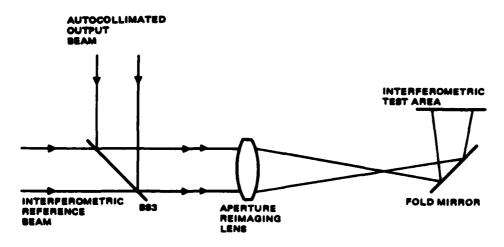
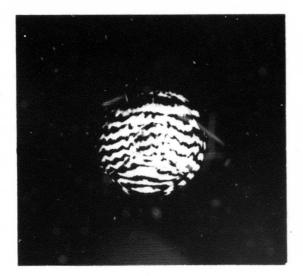


Figure 59. Modifications for output beam interferograms.

Note that the output wavefront is autocollimated back through the beam expander to the interferometric station. This double-pass configuration produces a phase error in the recorded output wavefront interferogram which is twice that existing in the true output wavefront. This doubling effect has been taken into account in the data reduction of the outgoing beam interferograms.

4.2.1 Nominal System

Interferograms of the output beam of the aligned HOLAB breadboard are shown in Figure 60. The interferograms in Figure 61 are of the sample beam



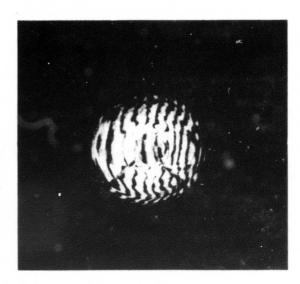
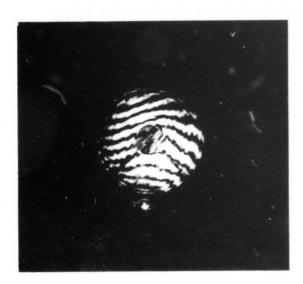


Figure 60. Nominal system output beam interferograms (double pass).



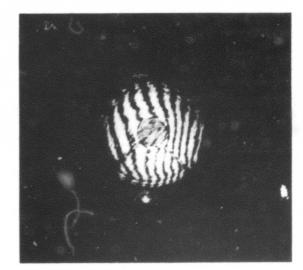


Figure 61. Nominal system sample beam interferograms (single pass).

of the nominal unperturbed HOLAB breadboard. The two dark radial lines in these and all the other interferograms are the shadows of the struts that support the folding flat mirror. The interferograms have been arranged such that the strut shadows, which are in the lower portion of the aperture, are in the lower portion of the photo.

Interferograms of the HOLAB beam expander optical components were provided by the optical vendor. Two orthogonal fringe orientation interferograms for the primary mirror are presented in Figure 62. The variations from straight, uniformly spaced fringes indicate departures from the ideal paraboloidal optical figure. In the double-pass interferometric test configuration used, a spacing variation of one fringe represents a primary mirror surface figure departure of 1/4 (0.6328) = 0.16 micrometer.

Two orthogonal fringe orientation interferograms for the primary and secondary mirror used together in a beam expander configuration are shown in Figure 63. In the double-pass interferometric test configuration used, a spacing variation of one fringe is twice the single pass wavefront departure at the test wavelength of 0.6328 micrometer.

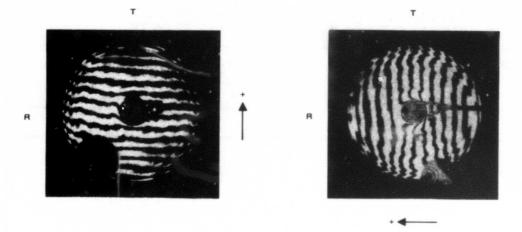


Figure 62. Primary mirror interferograms.

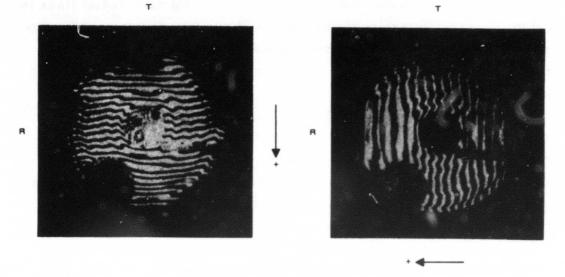


Figure 63. Beam expander interferograms.

The interferograms of Figures 61, 62, and 63 were measured for their departure from an ideal wavefront. The measurements are tabulated in Table 19. The wavefront produced by the primary mirror is dominated

TABLE 19. SYSTEM WAVEFRONT ERRORS; DEPARTURES FROM IDEAL WAVEFRONTS

Wavefront	Wavefront Error (Peak-to-Valley, Single-Pass at λ = 0.6328 μm)	
	Desired	Measured
Primary Mirror	≤ \(\lambda / 4\)	0.50λ (0.08λ RMS)
Primary + Secondary Mirror	≤ \(\lambda / \)2	0.64λ (0.13λ RMS)
Breadboard Output Beam	≤(3 / 4)λ	0.79λ (0.18λ RMS)
Breadboard Sample Beam	≤1λ	2.22\ (0.46\ PMS)

by several zonal optical figuring errors near the outside edge. The measured breadboard output beam wavefront is approximately that of the desired value. However, the breadboard sample beam wavefront is slightly more than twice that which is desired. The fan-shaped interference fringes indicate that the dominant sample beam wavefront error is astigmatic in character. Time and resources did not permit determining whether this error was due to fabrication, alignment, or mounting errors either before or after the production of the holographic grating on the primary mirror surface.

The breadboard was then utilized to obtain the following data on system performance with various system perturbations.

4.2.2 Focus Effects

Output beam and sample beam interferograms of focus effects produced by longitudinal translation of the secondary mirror and collimating lens relative to the primary mirror are shown in Figure 64. The top and third rows of photos in Figure 64 are interferograms produced by a longitudinal translation of only the secondary mirror in the direction away from the primary mirror. The second and fourth rows of photos are interferograms produced by longitudinal translation of both the secondary mirror and the collimating lens as a unit. If the collimating lens moves with the secondary mirror, the curvature of the sample beam wavefront is increased.

The effect on the sample beam wavefront when the collimating lens is longitudinally translated independently from the secondary mirror is demonstrated in Figure 65. These interferograms vividly point out the necessity for a rigid positioning relationship between the secondary mirror and the collimating lens. Otherwise, if the collimating lens were to translate independently, focus information would be contained in the sample beam wavefront which would be independent of that in the output beam.

The measured focus error of the breadboard outgoing beam and sample beam which is produced by motion of the secondary mirror along with the system optical axis is plotted in Figure 66. Clearly, a close correspondence exists between measured and predicted performance.

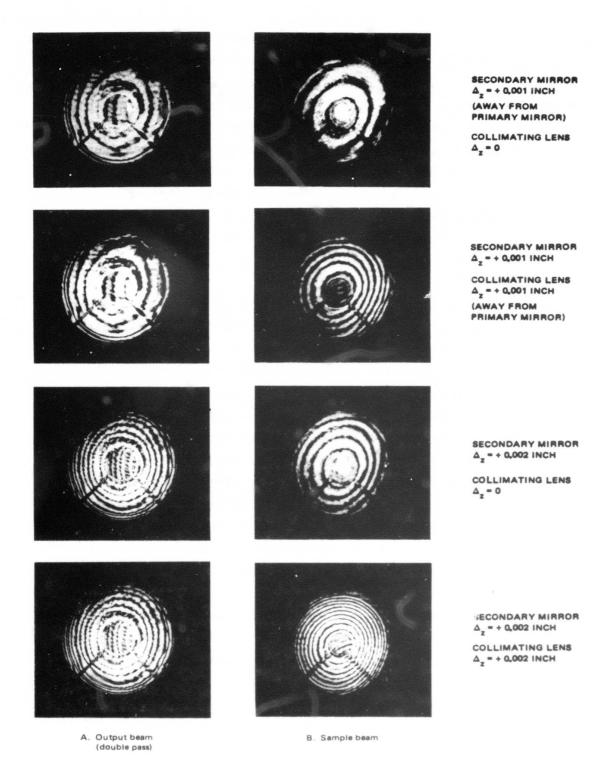
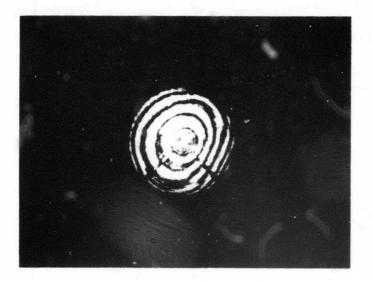


Figure 64. Secondary mirror and collimating lens focus effects.



 $\Delta_{_{\rm Z}}$ = + 0,001 INCH (AWAY FROM PRIMARY MIRROR)



Δ_z = + 0,002 INCH

Figure 65. Focus effects in sample beam due to collimating lens longitudinal motion (secondary mirror fixed at infinity focus.

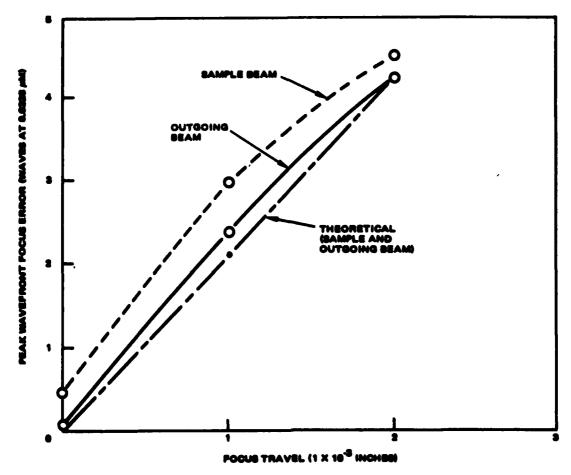


Figure 66. Focus effects, secondary mirror only.

The measured focus error of the breadboard outgoing beam and sample beam which is produced by the secondary mirror and collimating lens moving together along the system optical axis is plotted in Figure 67. The motion of the collimating lens introduces additional wavefront curvature into the sample beam. Therefore, this additional instrumental error would require proper processing to correctly relate sample beam focus error to outgoing beam focus error.

4.2.3 Decenter Effects

Beam expander misalignments produced by lateral translation of the secondary mirror and collimating lens and their effects on the output and sample beams are shown in Figures 68 and 69. The bottom row of

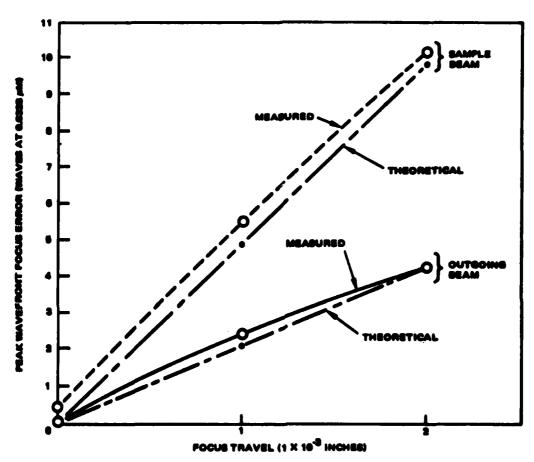
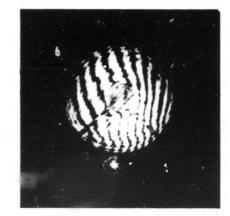
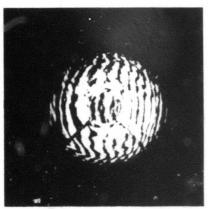


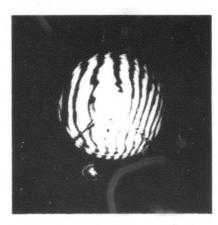
Figure 67. Focus effects, secondary mirror and collimating lens move together.





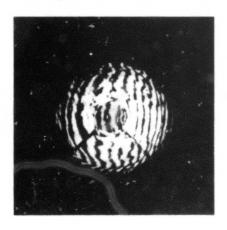
SECONDARY MIRROR $\Delta_{\chi} = 0$ COLLIMATING LENS $\Delta_{\chi} = 0$



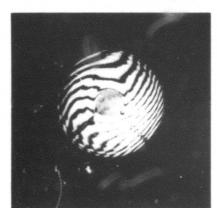


SECONDARY MIRROR $\Delta_{\chi} = +0,005$ INCH

COLLIMATING LENS $\Delta_{\chi} = 0$



 A. Output beam (double pass)

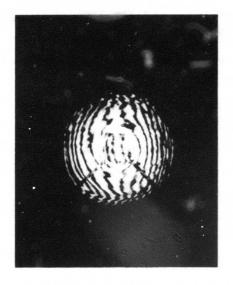


B. Sample beam

SECONDARY MIRROR $\Delta_{\chi} = + 0,005$ INCH

COLLIMATING LENS $\Delta_{\chi} = + 0.005$ INCH

Figure 68. Secondary mirror and collimating lens lateral translation effects.



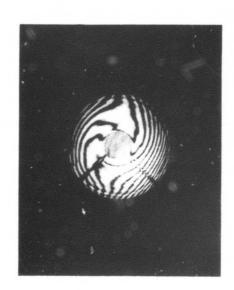


SECONDARY MIRROR 4 = + 0,010 INCHES COLLIMATING LENS $\Delta_{_{\rm X}}=0$

SECONDARY MIRROR A = + 0,010 INCHES COLLIMATING LENS Δ_x = + 0,010 INCHES



A. Output beam (double pass)



B. Sample beam

Figure 69. Secondary mirror and collimating lens lateral translation effects.

photographs in each figure shows the effect on wavefront of lateral translation of both the secondary and collimating lens as a unit.

The effect on the sample beam wavefront when the collimating lens is laterally translated independently from the secondary mirror is shown in Figure 70. The results confirm the system requirement that the collimating lens and secondary mirror not independently translate laterally.

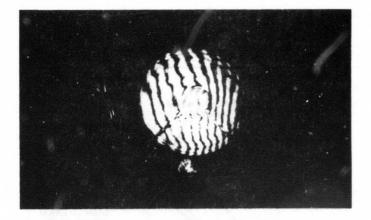
The measured coma error of the breadboard outgoing beam and sample beam which is produced by motion of the secondary mirror transverse to the system optical axis is plotted in Figure 71. Close correspondence between measured and predicted performance is demonstrated.

The measured coma error of the breadboard outgoing beam and sample beam which is produced by the secondary mirror and collimating lens moving together transverse to the system optical axis is plotted in Figure 72. The motion of the collimating lens introduces additional wavefront coma error into the sample beam. Therefore, this additional instrumental error would require proper processing to correctly relate sample beam coma error to outgoing beam coma error. However, a null-seeking system at the zero or minimum wavefront coma measurement position would properly correct any lateral displacement of the secondary mirror-collimating lens combination.

The measured coma error of the breadboard sample beam which is produced by the collimating lens alone moving transversely to the system optical axis is plotted in Figure 73. Again, a close correspondence between the measured results and predictions is shown.

4. 2. 4 Off-Axis Steering Effects

Interferogram effects produced by off-axis pointing of the output beam of the beam expander, and hence the sample beam, are shown in Figure 74. The HOLAB breadboard holographic sampling grating and collimating lens combination were designed to produce minimal sample beam wavefront phase error (<0.23 micrometer peak-to-valley) for off-axis pointing angles as large as 2 milliradians. Data in Figure 74 for off-axis output pointing angles of 0, 1, and 2 milliradians show only small changes in the output and sample beam wavefronts as expected.



COLLIMATING LENS $\Delta_{\chi} = 0$



4 - 0,005 INCH



A = 0,010 INCH

NOTE: SECONDARY MIRROR IN NOMINAL POSITION IN ALL PHOTOS

Figure 70. Collimating lens lateral translation effects on sample beam.

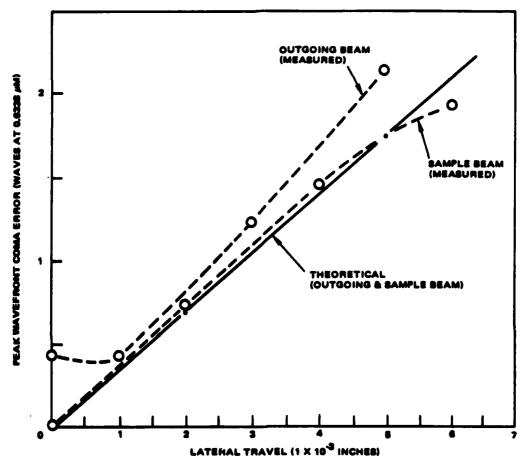


Figure 71. Decenter effects, secondary mirror only.

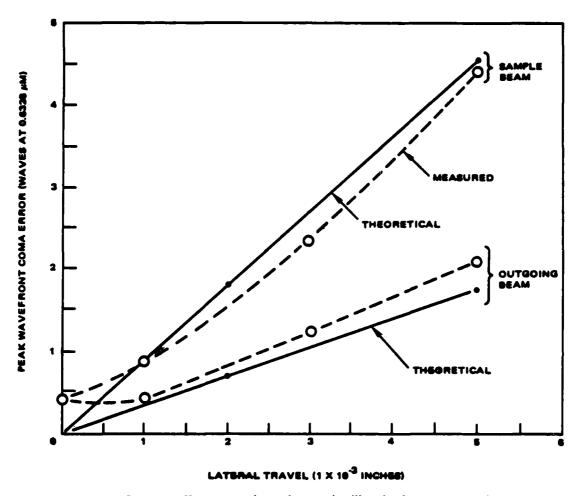
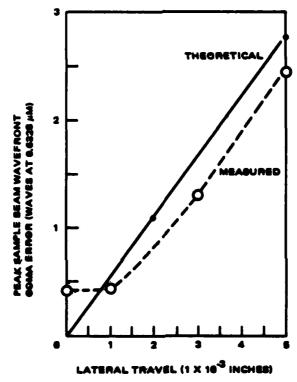


Figure 72. Decenter offects, secondary mirror and collimating lens move together



Pieure 73. Decenter effects, collimating lens only.

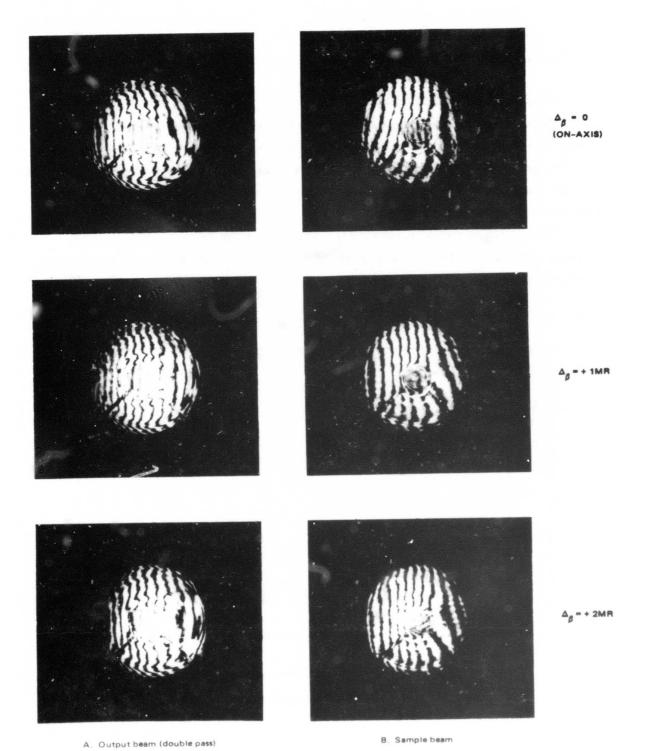


Figure 74. Beam expander off-axis steering effects.

The measured wavefront error of the breadboard outgoing beam and sample beam which is produced by off-axis pointing is plotted in Figure 75.

4.2.5 Substrate Deformation Effects

The effect on the output beam and sample beam wavefronts when the primary mirror substrate is deformed is shown in Figure 76. The technique used for deforming the mirror substrate is basically a pusher screw threaded through the back of the mirror cell. The screws then push on the back surface of the primary mirror in a single or multiplicity of locations. A deformation of the primary mirror substrate, and hence the holographic grating surface, results. The configuration of the deformation pressure points are given in Figure 77.

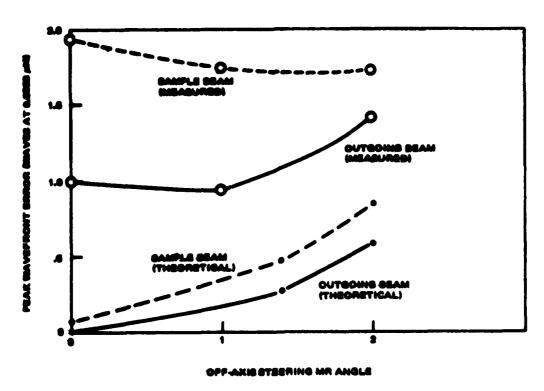


Figure 76. Off-axis steering effects

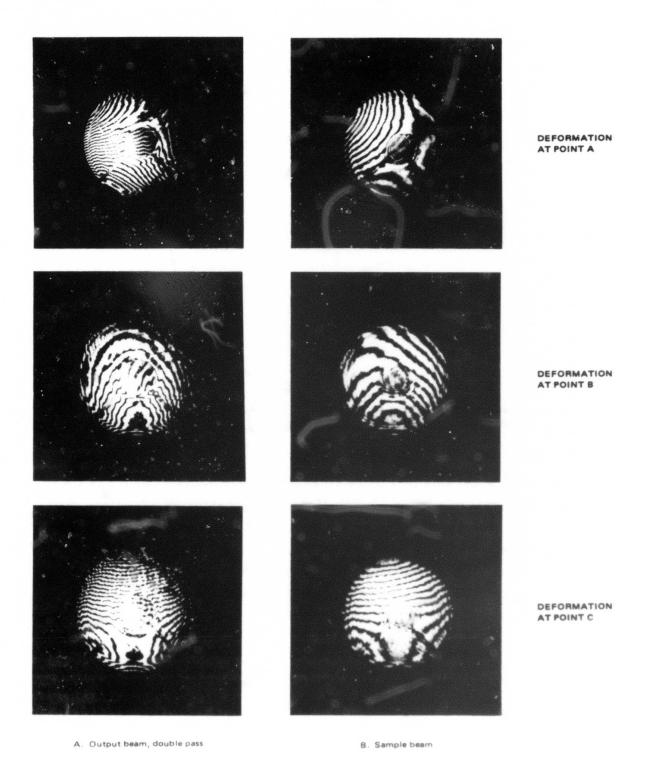


Figure 76. Primary mirror substrate deformation effects.

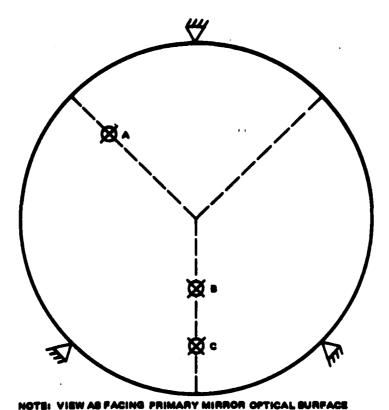


Figure 77. Primary mirror deformation device locations.

The interferograms of Figure 76 show that the sample beam has the same basic deformation profile as that of the output beam, as expected. The output beam interferograms contain twice as many fringes due to the double-pass configuration of the experiment.

The measured rms wavefront error of the breadboard outgoing beam and sample beam which is produced by deformation of the primary mirror substrate is plotted in Figure 78.

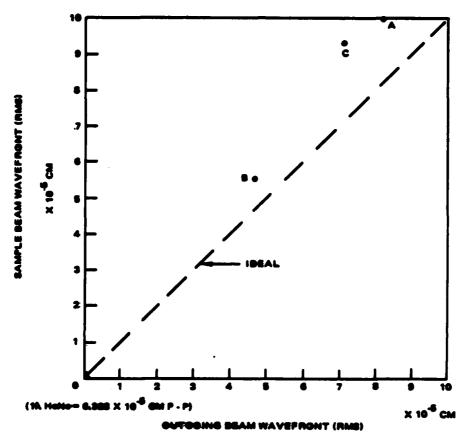


Figure 78. Primary mirror substrets deformation.

addresses	number of copies
James W. Cusack RADC/OCSE	5
RADC/TSLU GRIFFISS AFB NY 13441	1
RAUC/DAP GRIFFISS AFB NY 13441	2
ADMINISTRATOR DEF TECH INF CTR ATTN: DTIC-DDA CAMERON STA BG 5 ALEXANDRIA VA 22314	12
Hughes Aircraft Company Centinela and Teale Streets Culver City, CA 90230	5
AFML/ARAA Attn: Dr. J. Fender Kirtland AFB, NM 87117	1
AFVIL/ARAS Attn: Lt Col Paul Bovenkirk Kirtland AFB, NM 87117	1
The Aerospace Corp Attn: Dr. E.W. Silvertooth Bldg 110 MS 2339 PO Box 92957 Los Angeles, CA 90009	1

Attn: Emmanuel Goldstein 1401 Wilson Blvd Arlington, VA 22209	'
BDM Corp Attn: William Gurley 1820 Randolph Rd Albuqurque, NM	1
Charles Starke Draper Labs Attn: Frank Scammel 555 Technology Dr. Cambridge, MA 02139	1
Charles Starke Draper Labs Attn: Dr. Keto Soosar 555 Technology Dr MS 95 Cambridge, MA 02139	1
DARPA/DEO Attn: Col Ronald Prater Arlington, VA 22209	2
Eastman Kodak Attn: Robert Keim Kodak Aparatus Division 121 Lincoln Ave. Rochester, NY 14650	1
Eastman Kodak Attn: Richard Price KAL-Lincoln Park 901 Elmgrove RD Rochester, NY 14650	1

Itek Corp Attn: Roland Plante Optical Systems Division 10 Maguire Rd. Lexington, MA 02173 Lockheed Palo Alto Research Lab Attn: Richard Feaster 0/52-03, B201 3251 Hanover St. Palo Alto. CA 94304 Lockheed Space and Missile Co. Attn: Dennis Aspinwall Dept 5203 Bldg. 201 3251 Hanover St. Palo Alto, CA 94304 Lockheed Space and Missile Co. Attn: Dick Wallner Jept 5203 Bldg 201 3251 Hanover St. Palo Alto. CA 94304 MRJ Corp Attn: Dr. Kenneth Robinson 71 Blake St. Needham, MA 02192 NASA Ames 1 Attn: James Murphy MS 244-7 Moffett Field, CA 94035 NASA Marshall Space Flight Center 1 Attn: Charles (). Jones Mail Code EC32 Huntsville, AL 35812 Naval Sea Systems Command Attn: Dr. Saded Siahatgar PMS-405 NC 1 Room 11NO8

Washington, DC 20742

Naval Weapons Center Attn: Dr. H. Bennett Code 6018 China Lake . CA 93555 Perkin Elmer Attn: Dr. David Dean MS 241 Main Ave Norwalk, CT 06856 Perkin Elmer Attn: Henry Dieselmen 100 Wooster Heights Rd. Danbury, CT 06810 Riverside Research Institute Attn: Dr. Robert Kappesser 1701 N Fort Myer Dr. Suite 711 Arlington, VA 22209 SD/YNS Attn: Col H.A. Shelton PO Box 92960 Worldway Postal Center Los Angeles, CA 90009 University of Arizona Attn: Prof Robert Shannon %Charles Peyton Administration Bldg Tuscon, AZ 85721

W.J. Schaffer Assoc. Inc. Attn: Edward Borsare 10 Lakeside Office Park Nakefield, MA 01800

MISSION

of

Rome Air Development Center

RADC plans and executes research, development, test and selected acquisition programs in support of Command, Control Communications and Intelligence (C³I) activities. Technical and engineering support within areas of technical competence is provided to ESD Program Offices (POs) and other ESD elements. The principal technical mission areas are communications, electromagnetic guidance and control, surveillance of ground and aerospace objects, intelligence data collection and handling, information system technology, ionospheric propagation, solid state sciences, microwave physics and electronic reliability, maintainability and compatibility.

THE PROPERTY OF THE PROPERTY O